Design for bird strike crashworthiness using a building block approach applied to the Flying-V aircraft

Chen, Sian Ying; van de Waerdt, Wydo; Castro, Saullo G.P.

DOI
10.1016/j.heliyon.2023.e14723

Publication date
2023

Document Version
Final published version

Published in
Heliyon

Heliyon 9 (2023) e14723

Contents lists available at ScienceDirect

Heliyon

journal homepage: www.cell.com/heliyon

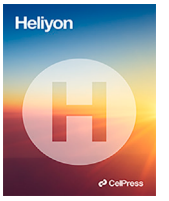

Research article

Design for bird strike crashworthiness using a building block approach applied to the Flying-V aircraft

Sian Ying Chen [a,b], Wydo van de Waerdt [a], Saullo G.P. Castro [b,*]

[a] Fokker Aerostructures B.V., Edisonstraat 1, 7903 AN Hoogeveen, the Netherlands
[b] Department of Aerospace Structures and Materials, Delft University of Technology, 2629HS Delft, the Netherlands

ARTICLE INFO

Keywords:
Crashworthiness
Bird strike
Design
Metallic
Aircraft design
Flying wing
Blended wing-body
Flying-V

ABSTRACT

The Flying-V aircraft concept promises better fuel-burn performance over conventional tube-and-wing configurations, integrating the passenger cabin and cargo volume into the lifting surface. However, the wing-fuselage and cockpit windows of the Flying-V are exposed to the flight direction, posing a new challenge to the design and certification of structures in terms of bird strikes. This study is a first step towards understanding the dynamic load path and contribution of each structural element on the bird strike resistance of the Flying-V leading-edge structures. The objective is to propose a building block approach to design the Flying-V's leading edge bird strike crashworthiness that complies with the EASA's certification CS25.631 using a 4lb bird impacted at a sea level cruising speed of 70 m/s. An additional requirement by the authors is to keep the structure within the elastic deformation during the impact of a 4lb bird to avoid the need for repairs in the Flying-V fuselage. Plasticity generated in the structure is regarded as damage and is used as a comparative parameter. At the highest building block level, a sensitivity analysis is performed to identify the effect of the thickness of each structural element on the plasticity and weight of the leading-edge structures. The trends are used to modify the baseline design and achieve a reduction of 80% of the plastic energy. The critical case of a 133 m/s impact of a 4lb bird at the cruise altitude of 37000 ft is also evaluated, and the results show penetration.

1. Introduction

1.1. The Flying-V concept and the challenge concerning bird strike

In aviation, a bird strike is a contact between a moving airborne vehicle and an avian animal. In conventional aircraft, bird strikes can be a significant threat to flight safety, causing damage to the aircraft's empennage, wing, windshield, and engine.

The Flying-V is a flying wing concept initially developed by Airbus and the Technical University of Berlin [4], promising an improvement of 20% in fuel burn performance compared to its conventional competitor aircraft, the Airbus A350. The Flying-V integrates the function of carrying the payload and fuel into its inboard wing-fuselage with the role of generating lift. Its outboard wing supports the control surfaces. Furthermore, the main landing gear bay combined with the engine pylon is installed in a large rear spar, which is also used to separate the pressured and non-pressured regions.

* Corresponding author.
E-mail address: S.G.P.Castro@tudelft.nl (S.G.P. Castro).

https://doi.org/10.1016/j.heliyon.2023.e14723
Received 6 July 2022; Received in revised form 7 March 2023; Accepted 15 March 2023

Available online 21 March 2023

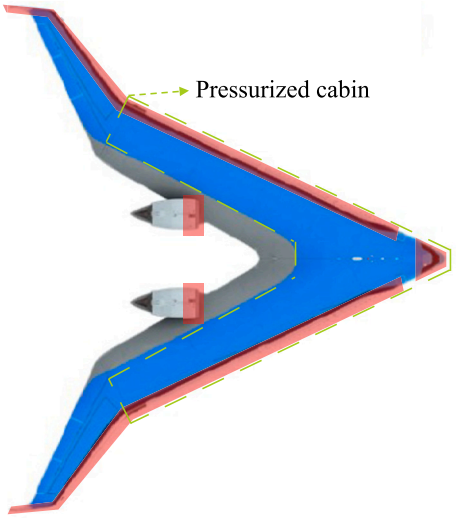

Fig. 1. Bird strike critical zone for the Flying-V.

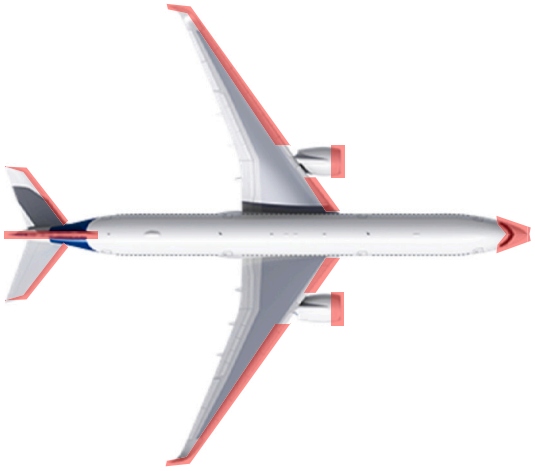

Fig. 2. Bird strike critical zone for the A350-1000, which has a wingspan of 64.75, comparable to the Flying-V.

In the inboard wing-fuselage, the cabin windows are located along the aircraft's leading edge, thus exposed to the flight direction as illustrated in Fig. 1. From the number of reported bird strikes between 2000 to 2014, the wing of a conventional plane has the highest number of reported bird strikes, while the impact on the pilot's windshield has the highest injuries and fatalities apart from the engines that were not in the scope [22]. From the reported results [22], the probability of bird strike can be deduced as the highest at the wing-fuselage of the Flying-V or similar blended wing body designs. The fact that the passenger's cabin windows are now located at the leading edge creates the logical expectation that injuries due to bird strikes will increase with the passengers seated next to the windows, contrarily to conventional planes, such as the A350 Fig. 2, where only the pilots are under risk of a direct injury due to bird strikes on windows. Therefore, there is a higher effect of bird strikes on the safety of the Flying-V when compared to conventional planes. Furthermore, the different impact scenarios create new load cases and failure modes that must be included in the preliminary design of this unconventional aircraft concept, given the high effect they will have on the final structural layout and weight. Therefore, in the present study, the cabin windows for the Flying-V are re-examined and re-designed, taking as a starting point the existing structural design proposed by Dotman (2021) [7]. The intended contributions are twofold:

- achieve a design for the cabin window structures that conforms to the EASA's certification CS-25 for large aeroplanes;
- for the impact scenario of a 2 lb bird at takeoff and landing speeds, achieve elastic bird strike resistance for the fuselage and window structures.

1.2. EASA certification for bird strike

For convenience, the certification specifications for bird strike from EASA CS-25 Amendment 26 are herein summarised [1]:

- CS 25.631 Bird strike damage: The aircraft must be designed to continue its safe flight and landing when a 4 lb bird strikes it with the flight speed of V_c at sea level or 0.85 V_c at 2438 m (8000 ft). The most critical speed should be chosen for the damage tolerance evaluation. Note that V_c is the cruising speed of an aircraft, which is related to flight altitude, aircraft specifications, and aerodynamic performance parameters.
- CS 25.775 Windshields and windows: Window panes and their supporting structures in front of the pilots should not be penetrated by a bird strike impact under CS 25.631. Note that this requirement will extend to all cabin windows in the case of the Flying-V.
- CS 25.775 Windshields and windows: The aircraft must be designed to minimise the damage of the flying window fragment to the pilots. The window should not be made of splintering materials. CS 25.775 must be shown for the transparent panes that appear in the front view of the aircraft and extend to all the cabin windows in the case of the Flying-V.

For the bird strike investigation in the Flying-V, the flight speed used for the critical damage location is V_c at sea level. The birds in the weight category of around 4 lb are gulls, ospreys, mallards, vultures, and similar. High-toughness materials such as aluminium alloys and polycarbonate are chosen as the window materials to minimise window fragmentation. Since the passenger windows are all visible from the front view of the aircraft, the passenger windows are herein treated as the standard pilot's windshield to comply with the EASA requirements.

Bird strike physical tests prove that the structure complies with the certification specifications. Wilbeck's team [28] carried physical bird-strike tests on rigid plates. The impact pressure history at the centre of the rigid plate was recorded, and theories were generated to predict pressure at different impact speeds and angles. Bird strike experiments are expensive in both cost and time. Therefore, the approach of virtual testing or certification by simulation should be used as much as possible based on validated results based on tests carried out by similar structures with sufficiently representative designs, and bird strike scenarios [1]. During the validation phase, the worst impact scenarios are identified from the simulation results, and the corresponding tests are proposed. After careful validation and the conclusion that test data support the simulation, the design space can be further explored using simulations to achieve a more optimum structural design. The present study is based on numerical models built to identify the critical design scenarios that the Flying-V team should test in the future.

1.3. Finite element approaches for bird strike

Different finite element (FE) approaches have been applied to simulate the structural behaviour under bird strike conditions. In mesh-based Lagrangian formulation schemes, each mesh node represents a particle with a fixed connectivity with one or more finite element types. The nodal accelerations are determined according to Newton's second law of motion. The forces acting on each node are calculated according to connected finite elements, external forces, and boundary conditions nonlinear change, which can result from element-to-element contact that develops throughout the dynamic analysis. With the progress of the simulation, the material points that are used to trace the deformation history will follow the structural deformation. However, in bird strike simulations, significant element distortions and the folding behaviour of the distorted elements make the element aspect ratio or skew level unacceptably high. It leads to poor numerical conditioning that might create spurious results or very small time step requirements that ultimately lead to a conditionally unstable simulation. To circumvent this issue, a common measure adopted by finite element solvers consists of deleting highly distorted elements. The elements that exceed the failure strain are removed from further time increments. However, this element removal directly violates the conservation principles of mass and energy [19]. According to Goyal et al. [13], this mass loss may result in excessive bird mass loss due to the bird's fluid behaviour, causing larger-than-expected distortions in the bird model and reducing the actual loads that are imprinted on the structures being investigated.

Eulerian approaches overcome the element distortion intrinsic to Lagrangian formulations by defining a mesh grid fixed in space that allows the material points to pass through, preventing the element from distortion. However, the Eulerian mesh requires a fine regular or voxelized mesh grid to properly represent complex shapes and complex boundaries to produce accurate results, which becomes computationally expensive [10].

Arbitrary Lagrange Eulerian (ALE) methods are a combination of the Lagrangian and Eulerian methods [3], where the reference coordinate is arbitrary and, depending on the motion, the calculations are: Lagrangian-based, with the nodes moving together with the material points; or Eulerian-based, with the nodes fixed and the material points moving through the mesh. One of the significant disadvantages of the ALE method is that the user must empirically determine the optimal mesh motion [12].

Smoothed particle hydrodynamics (SPH) is a mesh-free Lagrangian method in which particles are directly used to represent the material points without fixed connectivity, as in the case of finite elements. The internal forces are calculated based on the interactions with adjacent particles that fall within the so-called smoothing length, which is related to the spherical radial distance in which a particle can influence adjacent particles. Being a Lagrangian method, it keeps some crucial advantages, such as efficient tracking of the material deformations and history-dependent behaviour [13]. Compared to FE, two main disadvantages of SPH are that searching for the nearest particles is costly and that an accurate representation of surface boundaries is impossible. However, SPH becomes an acceptable method to model a bird while assuming it behaves like a fluid during the bird strike event. Representing a bird using a cloud or blob of particles within an SPH scheme is advantageous in terms of conservation of mass and energy, given that the mesh-free behaviour allows the solution involving irregular geometries that produce any free-surface fluidic behaviour without element distortions or tangling. SPH also has a higher accuracy by following the bird's flow path after impact, which is useful when there are other impacts and interactions with the structure in the vicinity of the first impact location. In the present study, the SPH method is used to simulate the bird, whereas FE is used to simulate the Flying-V structures.

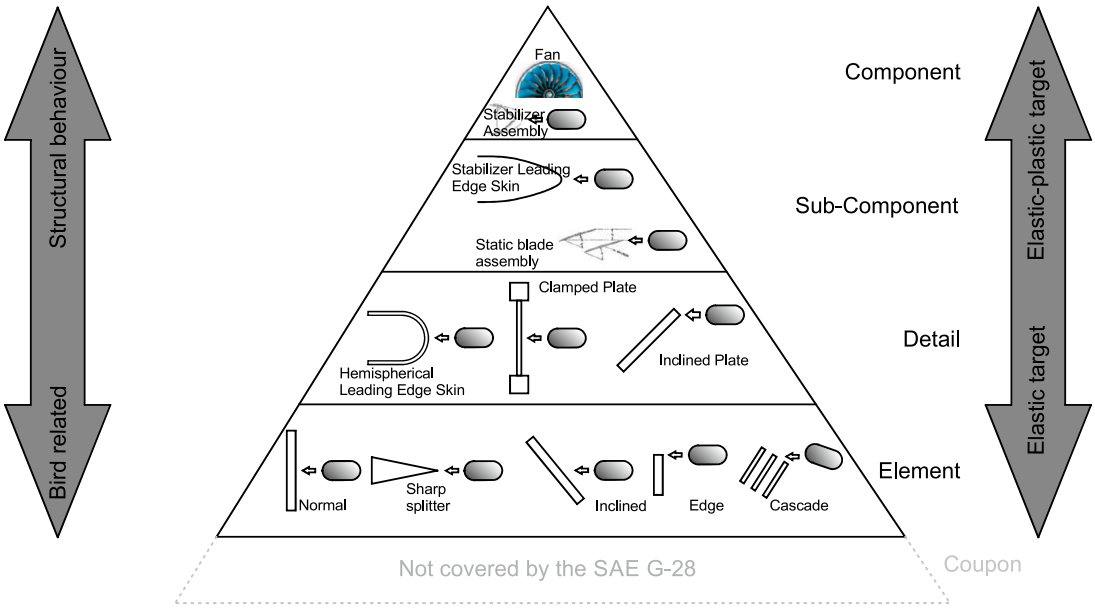

Fig. 3. Building block approach for the bird strike investigation [24].

1.4. Building block approach

According to EASA's Modelling & Simulation of CS-25 Structural Certification Specifications, The building block approach (BBA) is used as a design methodology to obtain accurate numerical structural models validated by experimental tests [2]. This method has been implemented in the industry by Heimbs et al. and Doubrava et al. to produce reliable impact simulations for aerospace composite components to reduce the physical tests [14,9,8]. Based on their successful implementation, in our study, the building block approach is implemented in designing novel aircraft assembly structures instead of individual components. On each level of the BBA, structural data is produced from physical tests and numerical results that start from defining the material coupon, structural element, detailed model, sub-component, full-component to full-aircraft. Physical tests and numerical results are compared to achieve accurate simulation by isolating erroneous results. An illustration of the bird strike's BBA of a stabiliser's leading edge and the engine blades is shown in Fig. 3, created under SAE G-28, Simulants for Impact and Ingestion Testing [24]. It is unnecessary to impact full-aircraft with the bird for bird strike impacts. Instead, a structural component representing the affected region by bird strike will suffice.

The SAE G-28's building block approach presents the lowest level of coupon testing. The materials for the structure and the bird's behaviour are characterised, and their corresponding numerical models are selected and validated. As for the bird representation, using actual bird carcasses for impacts has disadvantages such as lack of hygiene and significant variations of the bird density distribution [26,28]. These variations also depend on the bird species, significantly affecting the impact behaviour of the structures. Therefore, substitute bird materials and geometry were developed on the coupon level to mimic its behaviour while providing a more controlled projectile. Gelatin has been accepted as a material representing a bird, being considered a superior projectile by most studies [26,28]. The variables that determine the property of the gelatin bird are chemical formulas, void contents, and reinforced structures [26,28].

The element level, the second level of the building block approach, determines the bird's material behaviour when it is impacted on clamped, metallic rigid plates with different scenarios. The impacted plate deforms in the elastic region and acts as a damage indicator to show the equivalence between a real bird and an artificial bird's impact. Pressure, force, and strain history are recorded for different bird materials. There are four stages of the pressure history: The initial peak pressure, the pressure decay region, the steady pressure region, and the termination point, representing the end of impact [28]. Split, edge, and cascade impact tests are methods to examine the engine blades' bird strike effect in the case of bird impact with engine fan blades.

The third level of the building block approach is the detailed level analysis. The impacted structure is no longer considered a rigid body, so its thickness is reduced to a more realistic value. Plastic deformation is commonly introduced into the model, while the impact scenarios still involve simplified geometries. The fourth level is the sub-component assembly. The simulations and tests already adopt a partial section of the leading edge model. The projectile is being impacted to the same configuration and thickness as the actual structure component, which includes assembly elements such as fasteners and some representative reinforcements such as stiffeners and ribs. Finally, at the component level, the projectile impacts the entire assembly of the leading edge or any other structure, such as a rotating engine. At this stage, there is a high maturity in validated modelling capability that covers a broad range of geometries and impact scenarios.

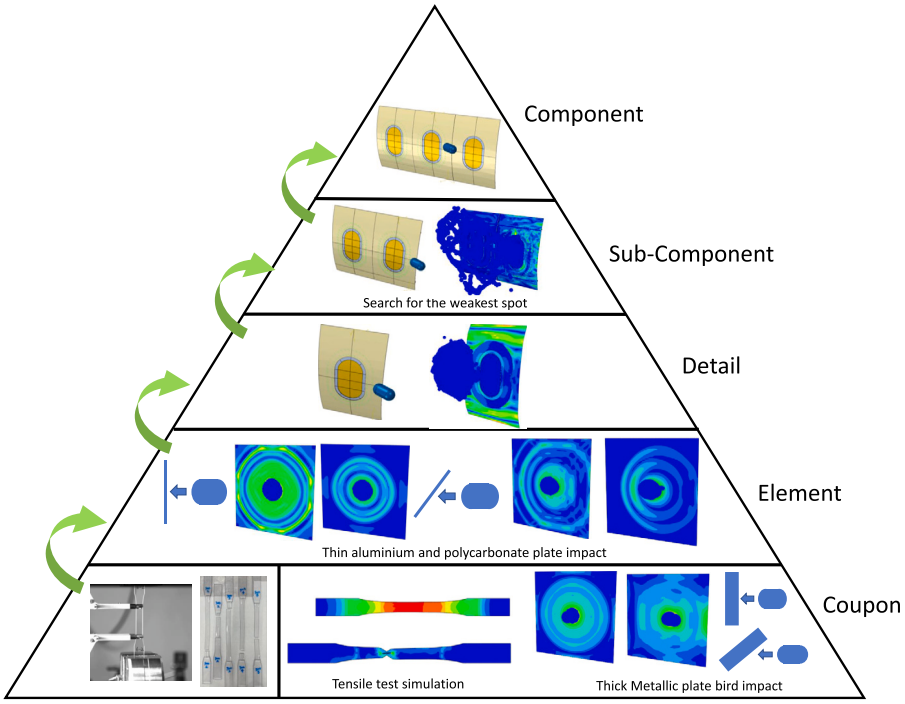

Fig. 4. Bird strike BBA road-map for the Flying-V.

2. Methodology

2.1. Building block approach of the Flying-V

Fig. 4 shows the proposed building block approach (BBA) for the bird strike assessment of the Flying-V wing-fuselage leading edge windows. Compared to the SAE G-28's BBA, which characterises the bird's material behaviour at the element level, the task at this level is moved to the coupon level, where the materials are characterised. The relocation of the level is due to the detailed level of the Flying-V's BBA has been used for the impact of a structural assembly of aluminium structures and a polycarbonate window. The thin-plate impact testing at the detailed level of SAE G-28 will thus be moved to the element level in this study.

The simulations performed on each level and herein demonstrated should be supported by physical tests. However, this study is part of the preliminary design of the Flying-V aircraft, only the simulations of the polycarbonate material are compared with physical tests. On the coupon level, the properties of aluminium alloy 7050-T7451, cladded aluminium 2024-T42, bird material impact behaviour, and polycarbonate sheets are defined in the simulation model and validated utilising literature. The bird material's deformation and stress behaviour is studied by impacting it on a 25-mm thick aluminium 2024-T42 plate at 70 m/s.

At the element level, the normal and inclined impact of the bird is performed on 3-mm thick aluminium 2024-T42, 7050-T7451 and polycarbonate plate, with a speed of 70 m/s. A 9.6-mm polycarbonate impact is also simulated to reduce its plasticity. The maximum pressure-time history is recorded and presented. The element level aims to examine the structural impact behaviour using a more realistic thickness.

On the detailed level, one window section is impacted by a 4 lb bird with a speed of 70 m/s. The distribution and the values of the stress and plastic strain are examined throughout the impact history. Structural components fixated together by tie constraints for impact simulations in Abaqus. On the sub-component level, two window sections are presented. Fuselage frames, stringers, the whole window configuration, and fasteners are added to this level to perform a more rigorous investigation of the bird strike. The goal for the sub-component level is to search for the impact location that generates the maximum plastic strain energy by impacting the bird model on multiple locations on the fuselage frame and the window structure. The thicknesses of the window structure components are adjusted in a sensitivity analysis to determine which component can contribute the highest decrease in plasticity.

Furthermore, the 4 lb bird with a cruising speed of 37000 ft (the highest flight altitude ever recorded for a bird strike) is impacted on the critical location of the window. Simulations performed at the component level with three window sections are left for future work when more information about the Flying-V geometry and design is available. To validate the simulation models, the Flying-V's window structure should be tested with a bird strike on the component level. After that, more simulations could be done by impacting different locations, bird masses, and impact speeds. At such a level of validated modelling, the simulation results could be used to support the Flying-V certification campaign.

Table 1
Material properties of the aluminium alloys used in the wing-fuselage and window frame structures.

Aluminium Alloy	7050-T7451	7075-T7351	Alclad-2024-T42
Density (kg/m^3)	2800	2800	2770
Elastic Modulus (MPa)	71000	71000	68300
Poisson Ratio	0.33	0.33	0.33
Fracture Strain	0.08	0.07	0.2
Fracture Energy (J/m^2)	112000	110000	12700
Softening Behaviour	Exponential	Exponential	Exponential

2.2. Material properties

The aluminium alloys' properties are applied to the Flying-V's wing-fuselage and window structures. The material data from the fasteners are obtained from Fokker Aerostructure's material database. The Polycarbonate material properties used for the passenger window pane are obtained from experiments, and the bird material data, represented as gelatin, is obtained from the literature. This sub-section is dedicated to detailing all the aforementioned material properties.

2.2.1. Aluminium alloys for the wing-fuselage and window structures

Table 1 provides the material properties for the aluminium alloys 7050-T7451, 7075-T7351, and cladded aluminium 2024-T42. The actual values for the fracture strain and fracture energy obtained from Fokker Aerostructure's material database are not provided for confidential reasons. The values herein published are representative and rounded up to the second digit after the decimal point for the fracture strain; and to the fourth digit for the fracture energy. In this study, the strain rate dependency is not considered since not using the strain rate dependency creates a conservative simulation answer for metal and joints, which is preferred for the certification approach.

In Table 1, the ductile damage behaviour of aluminium alloys contains the fracture strain and fracture energy. Ductile damage in Abaqus is initiated after the true stress reaches the material's yield stress with a zero plastic strain.

After the alloys are loaded beyond the ductile damage initiation point, the yield stress's softening and the elastic modulus degradation initiate until the effective load-carrying capacity reaches zero. The corresponding point where the load reaches zero and the material fractures are defined as the failure strain or the fracture strain shown in Table 1. If element deletion, an available resource in Abaqus, is activated for the model, the element is deleted at the fracture strain point. The stress-strain curves of the three aluminium alloys can be found in the Metallic Materials Properties Development and Standardization (MMPDS) handbook [15], which are equivalent to the actual properties used in this project. The fracture toughness (K_{IC}) is indicated for the three alloys, which can be calculated into fracture energy (G_{IC}) using Equation (1):

$$G_{\mathrm{IC}} = \left(1 - \nu^2\right) K_{\mathrm{IC}}^2 / E \tag{1}$$

where: E given in [MPa], and ν, are respectively the elastic modulus and the Poisson ratio of the material; K_{IC} given in [MPa$\sqrt{\mathrm{m}}$] is the fracture toughness which can be measured by using compact tension (CT) coupons tests. Using the fracture toughness (G_f) as a damage evolution parameter in Abaqus creates a stress-displacement response after the softening initiation rather than a stress-strain response. This is an advantage since the stress-strain response cannot accurately present the material's behaviour during softening due to its dependency on the mesh size.

The stress-strain curves are also provided as figures in which data points can be extracted and transformed into true stress-strain curves. Comparing the three alloys in Table 1 and using the MMPDS handbook, the cladded aluminium 2024-T42 has the highest fracture toughness. Aluminium 7075-T7351 and 7050-T7451 have a higher tensile strength than 2024 but a lower fracture toughness. They have similar elastic properties, and 7050-T7451 has higher toughness and tensile stress. Therefore, the two aluminium alloys that are used in the model are aluminium 2024-T42 and 7050-T7451.

2.2.2. Gelatin material for the bird's representation

To define the bird gelatin material in Abaqus using Smoothed Particle Dynamics (SPH), one needs to define the density and an equation of state (EOS) that relates the density with the isostatic pressure. Although birds have different shapes among different species, the density of all the birds is close to 950 kg/m^3, which is customarily considered uniform throughout the bird [23]. The main content of the bird is water, and its viscosity and strength can be neglected during impact. Therefore, the bird behaves like a fluid during impact, giving a hydrodynamic response to the structure. Regarding the EOS, the $U_s - U_p$ is adopted in Abaqus/Explicit, which describes a linear relationship between the shock velocity U_s and the particle velocity U_p. The $U_s - U_p$ method in Abaqus defines a pressure for materials in compression as Equation (2):

$$p = \frac{\rho_0 c_0^2 \eta}{(1 - s\eta)^2}\left(1 - \frac{\Gamma_0 \eta}{2}\right) + \Gamma_0 \rho_0 E_m \tag{2}$$

where: ρ_0 is the reference density when the medium has no pressure; η is the nominal volumetric compressive strain $1 - \rho_0/\rho$; ρ is the current density that varies during the impact time; Γ_0 is a material constant; E_m is the internal energy per unit mass; s is a constant

Table 2
Gelatin material properties used in Abaqus for the bird representation.

Properties	Value
ρ_0 (kg/m^3)	950
c_0 (m/s)	1480
s	0.92
Γ_0	0.1

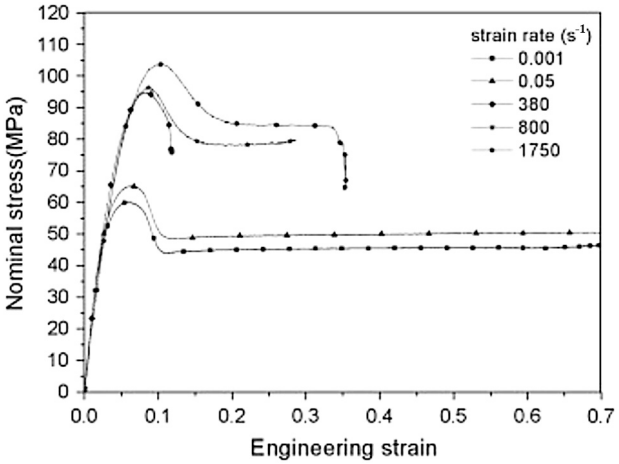

Fig. 5. Tensile stress-strain curves at different strain rates [11].

Table 3
Tensile test planning.

Testing Machine	Loading Rate (mm/min)	Strain Rate (%)	Number of Coupons
ZwickRoell 20 kN	6	0.0009	5
ZwickRoell 20 kN	300	0.0432	5
ZwickRoell 20 kN	750	0.1058	5
MTS 15 kN	7500	1.0897	2
MTS 15 kN	15000	2.2015	2
MTS 15 kN	30000	3.1207	2

that defines the linear $U_s - U_p$ slope; and c_0 is the speed of sound in the medium. The properties of the bird used in Abaqus are shown in Table 2. The data is based on the Mie-Grüneisen EOS's parameters for water [23,27].

2.2.3. Polycarbonate material for the window pane

The polycarbonate material from Arla Plast MAKROCLEAR™ is used for the window pane. The stretched polycarbonate sheets have ten times the impact strength of a high-impact PMMA and similar density. The density and the fracture energy used for the polycarbonate material properties in Abaqus come from a data sheet [21]. The elastic, plastic, and ductile damage properties; are determined by tensile testing, as described next.

Polycarbonate is a strain rate-dependent material for which the material properties at low strain rates are obtained according to the ASTM D638standard test method for the tensile properties of plastics, which is a quasi-static tensile test that is applicable only to strain rates less than 0.25 s^{-1}. However, high-speed bird strike impact requires material properties corresponding to strain rates of thousands of strain units per second. Fu et al., Cao et al., and Kendall et al. [11,5,16] performed dynamic tensile tests at high strain rates by using a split Hopkinson tension bar (SHTB) system. The result of Fu et al. is shown in Fig. 5. The results showed that the polycarbonate material has an elastic and plastic behaviour stage. Strain softening occurs after the yield point, and the yield stress is sensitive to the strain rate. The yield stress increases when the strain rate increases while the failure strain decreases. The Young's modulus is independent in their result, while Kendall et al. and Xu et al. [16,29] reported an increasing elastic modulus when the strain rate increases.

The tensile testing of the polycarbonate is performed according to the ASTM D638 standard test method, and the dimensions for a type-I polycarbonate coupon with a thickness of 5 mm are shown in Fig. 6. The tensile test plan is presented in Table 3.

According to ASTM D638, each loading rate is tested with five coupons, performed with the ZwickRoell machine. Only two coupons were tested for the MTS machine since the high loading rates are not within the range of the standard. The tensile testing is recorded with a camera for 6, 300, and 750 mm/min loading rates and a high-speed camera for 7500, 15000, and 30000 mm/min.

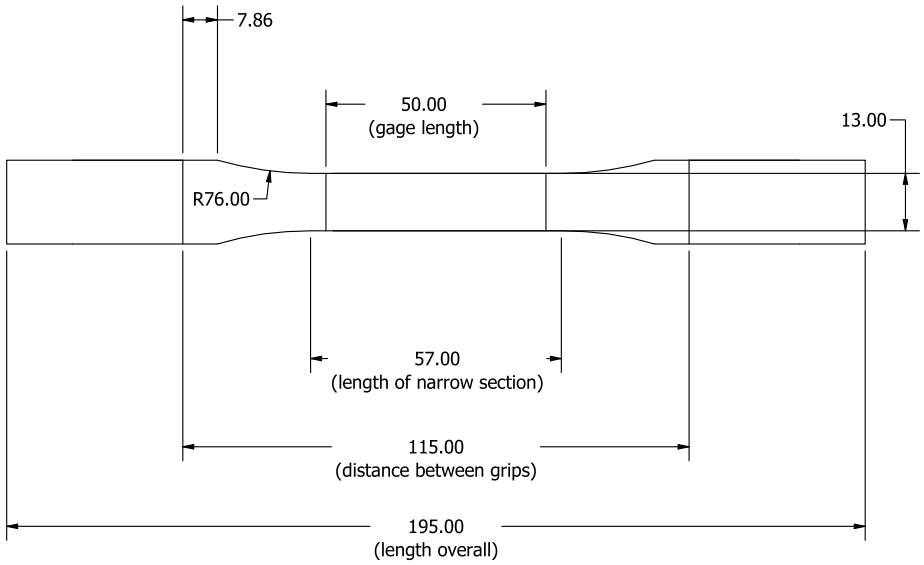

Fig. 6. Polycarbonate coupon dimensions (in mm) [6].

Table 4
Assigned velocity for simulation tests.

Strain Rate (s^{-1})	0.001	0.04	0.11	1.09	2.20	3.12
Assigned Velocity (m/s)	0.000115	0.0046	0.01265	0.12535	0.253	0.3588

A sensor arm extensometer is applied to only the lowest loading rate coupons at 6 mm/min (0.001 s^{-1}) to measure the displacement starting from the initial 50-mm gauge length. For the other loading rates, the displacement values are achieved from the machine's displacement sensors rather than the sensor arm extensometer to avoid damaging the extensometer at high loading rates.

The maximum tensile strain rate is limited to 3 s^{-1}, which is still not high enough to present the polycarbonate behaviour at high impact speeds. Therefore, stress-strain properties for high strain rates more compatible with the bird strike impact are determined based on the results from Fu et al. [11]. The cross-section dimensions of the narrow coupon sections are measured before the test and later used for determining the engineering stress. Force and displacement data are recorded during testing. To plot the nominal stress-strain curve, the force data is divided by the unloaded cross-section of each coupon. The nominal strain data are computed by the grip displacement divided by the defined initial length. It should be mentioned that in the actual setup of the testing machine, we had to keep the distance between grips to 135 mm instead of the 115 mm shown in Fig. 6. This is due to the 3-mm instead of 4-mm clamping depth limit on each grip side. This did not affect the calculated strain because the cross section within the region of the 10-mm clearance on each side of the specimen did not change its geometry during the entire test history. This is shown in detail in the testing videos provided in a data set [6]. Therefore, the defined initial length for the nominal strain calculation is 50-mm gauge length for 6 mm/min (0.001 s^{-1}) and 115 mm for the rest loading rates. The 6 mm/min loading rate extensometer data will determine the elastic modulus.

The true stress and true strain are calculated to determine the level of plasticity using Equation (3). The plastic strain ε^p is then computed by Equation (4); where ε^t is the total strain that equals the true strain ε.

$$\begin{aligned} \varepsilon &= \ln\left(1+\varepsilon_{\text{nom}}\right) \\ \sigma &= \sigma_{\text{nom}}\left(1+\varepsilon_{\text{nom}}\right) \end{aligned} \tag{3}$$

$$\varepsilon^{pl} = \varepsilon^t - \frac{\sigma}{E} \tag{4}$$

A coupon model is constructed in Abaqus using the same geometry and experimental setting. The material data of this coupon model contains experimentally determined and literature obtained [11] material properties of all the different strain rates. This coupon model is elongated at the same engineering strain rates as the experiments to compare and validate with the experimental nominal stress-strain curves.

A dynamic, explicit analysis uses eight-node linear brick elements with reduced integration. For the boundary conditions, the first clamping end is set as encastered. The displacements are only allowed in the loading direction at the second clamping end. The clamp-to-clamp distance is 135 mm. A prescribed velocity is assigned to a reference point at the second clamping end shown in Table 4. The reaction load at the first clamping end is recorded each time interval. The reference points' reaction force and displacement history at the clamping ends generate the nominal stress-strain curve. The nominal stresses are determined by dividing the reaction force by the narrow section's cross-section. The nominal strains are determined by dividing the displacement by the 115-mm defined in Fig. 6. The finite element model is shown in Fig. 7.

Fig. 7. Finite element model of the polycarbonate coupon.

Table 5
Flying-V parameters.

MTOW (kg)	$266(10^3)$
b (m)	65
S (m^2)	886.66
$C_{D,0}$ (Counts)	54.3
Lift-to-drag-ratio	21.7
e	0.811
$\rho_{air,0}$ (kg/m^3)	1.25
$\rho_{air,8000}$ (kg/m^3)	0.9638
$\rho_{air,37000}$ (kg/m^3)	0.36976
AR (m)	4.7651
f_{carson}	1.32
Sweep Angle	63.5°

2.3. Impact scenarios

According to the FAA database from 2000-2014 [22], 70% of the bird strikes occurred at an altitude below 500 feet (152.4 meters). Aircraft at heights between 0 to 100 feet (30.48 meters) constitute more than 60% of registered aircraft destruction. Among the bird strike cases recorded during flight [22], over 90% of the cases occurred during the approach, landing roll, take-off run, and climb. According to the high probability of the bird striking at aircraft height and flight phases, the impact velocity studied in this project is the approach and take-off speed of the Flying-V.

The Flying-V's parameters are shown in Table 5 [20] to calculate the cruise speed at different altitudes.

Three cruise speeds are calculated at sea level, 8000 feet (2438.4 meters) and 37000 feet (11277.6 meters). The EASA requirements calculate sea level and 8000 feet altitudes. The 37000 feet altitude is the highest altitude ever recorded for a bird strike.

The lift coefficient of the wing is calculated by Equation (5):

$$C_{L,altitude} = \frac{MTOW}{\frac{1}{2}\rho_{air,altitude} V_{c,altitude}^2 S} \tag{5}$$

Using $C_{L,altitude}$, the drag coefficient $C_{D,altitude}$ can be calculated by Equation (6),

$$C_{D,altitude} = C_{D,0} + \frac{C_{L,altitude}^2}{\pi e AR} \tag{6}$$

where $C_{D,0}$ is presented in counts, one count is 0.0001. Therefore the value of $C_{D,0} = 0.0054$. After obtaining the lift and drag coefficient, the cruising speed $V_{c,altitude}$ can be calculated using the lift and drag coefficient ratio shown in Equation (7).

$$\frac{C_{L,altitude}}{C_{D,altitude}} = 21.7 \tag{7}$$

The cruising speed of the three altitudes is shown in Equation (8)

$$\begin{aligned} V_{c,0} &= 71.126 \text{ (m/s)} \\ V_{c,8000} &= 80.228 \text{ (m/s)} \\ V_{c,37000} &= 133.38 \text{ (m/s)} \end{aligned} \tag{8}$$

According to EASA CS25.631, $V_{c,8000}$ times 0.85 is approximately 68.2 (m/s), lower than $V_{c,0}$. Thus, the bird strike velocity applied in the simulations is the V_c at sea level rounded to the nearest ten as 70 m/s.

2.4. Bird strike simulation in the building block approach

2.4.1. Coupon level

The coupon level contains the impact of the bird model against a rigid flat plate model. Studying the bird impacting a rigid plate gives a better understanding of the bird deformation corresponding to its materials and also the interface stress generated with the target. Various geometries such as ellipsoid, hemispherical-ended cylinder, straight-ended cylinder, and sphere are proposed for the bird's geometry. The comparison of pressure history between different geometries with the experiment is shown in Fig. 8. It can be seen that the straight-ended cylinder had the highest pressure, and the hemispherical-ended cylinder had the closest Hugoniot pressure compared to the experiment test. However, it is still four times higher. Despite this, the hemispherical-ended cylinder geometry is still the most common geometry used to represent bird strike, and therefore it is the chosen representation for the bird geometry.

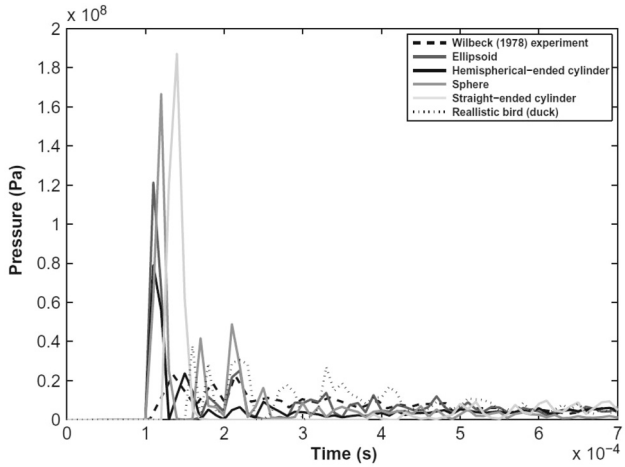

Fig. 8. Centre impact pressure history of the four geometries. [23].

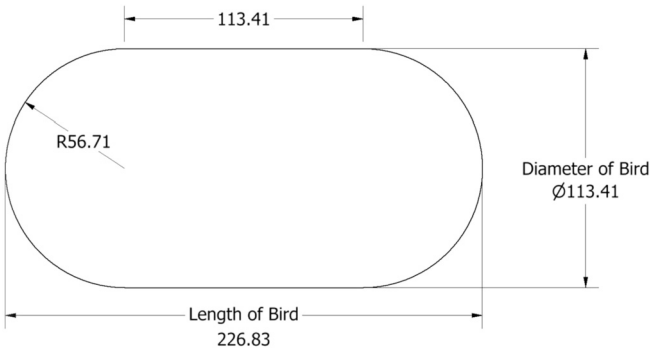

Fig. 9. 4 lb bird model dimensions (mm).

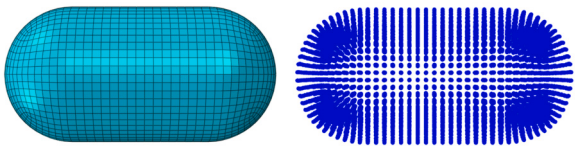

Fig. 10. Bird's model conversion to particles by SPH method.

For the hemispherical-ended cylinder, the length-diameter ratio is set to be two [23]. With a bird mass of 4 lb (1.814 kg) and density of 950 kg/m^2, the volume can be calculated as 1.91×10^{-3} m^3. The radius of the hemispherical-ended cylinder R_{bird} can be determined from Equation (9):

$$\begin{aligned} \tfrac{4}{3}\pi R_{bird}^3 + 2\pi R_{bird}^3 &= 1.91e-3 \\ R_{bird} &= 0.0567 \text{ (m)} \end{aligned} \tag{9}$$

The bird model is constructed using R shown in Fig. 9.

The bird geometry is first approximated using hexahedral C3D8R Lagrangian finite elements, which are then converted to SPH particles using a time-based criterion. At the beginning of the impact event, a time threshold of 0 (zero) is specified to convert all the parent elements to particles. The PPD (particles per isoparametric direction) defaults as 1 (one). The bird's mesh and its conversion to particles are illustrated in Fig. 10.

For the plate model, the material selection will not affect the bird's behaviour as long as the plate is thick enough to prevent plasticity and with small deformations that can be neglected. Therefore, an aluminium 2024-T42 plate model consisting of a one-meter by one-meter square deformable shell with a thickness of 25 mm is created. The boundary conditions are clamped at the four edges. In the Abaqus software, element deletion for the plates is activated. The sea level cruising speed of 70 m/s is tested for impact. The normal impact of the plates with an inclination of 63.5 degrees with respect to the impact direction is performed, which corresponds to the sweep angle of the Flying-V leading edge.

The model set-up table is shown in Table 6. The normal and inclined impact model boundary conditions are shown in Fig. 11.

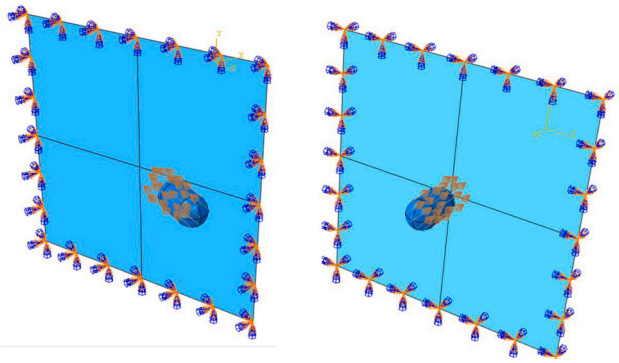

Fig. 11. Coupon level, inclined and normal impact load and boundary conditions.

Table 6
Coupon level model information.

Model	Bird	Plate
Shell Thickness (mm)	–	25
Material	- Gelatin	- Aluminium 2024-T42
Mesh element Type	- Explicit, Linear - C3D8R - Conversion to Particles: On - Time based criterion - Time threshold: 0	- Explicit, Linear - S4R - Reduced integration: Off - Element Deletion: On
Element Global Size (m)	0.0065	0.015

Table 7
Element level plate model information.

Material	Aluminium 2024-T42	Aluminium 7050-T7451	MAKROCLEAR Polycarbonate
Shell Thickness (mm)	3		
Mesh Element Type	- Explicit, Linear - S4R - Reduced Integration: Off - Element Deletion: On		
Element Global Size	0.015		

2.4.2. Element level

The element level uses an identical Abaqus model as the coupon level's thick plate impact. On this level, the study object is the plate's behaviour rather than the projectile's. The plate is reduced to a more realistic 3-mm thickness, and different plate materials are studied, shown in Table 7. Normal and a 63.5-degree inclined impact at 70 m/s is performed. The impact history's maximum Mises stress, internal energy (ALLIE), and plastic strain energy (ALLPD) are determined.

2.4.3. Detail level

The detailed level uses a window design modified from the publicly available patented passenger window from Mitsubishi Aircraft Corporation as a starting design reference since it clearly shows all the constituents of a passenger window [17]. A simplified window representation with three components is proposed on this level: one layer of polycarbonate pane, a window frame, and a fuselage skin. The rubber gasket seal and fillets are ignored, and the fasteners are simplified as tie constraints. The skin is set to be 2.5 mm thick, and the rest of the window component cross-sections are traced based on the full-scale dimensions provided by Mitsubishi Aircraft Corporation [17]. The tapered window frame geometry is simplified as a flat surface, and the thicknesses of the components are homogeneous. The fuselage skin section has a frame pitch of 635 mm with a leading-edge cylindrical curvature of 1.25 m. The model is shown in Fig. 12 with a window size of 0.244 m horizontal width and 0.44 m vertical height (0.244 m x 0.44 m). The

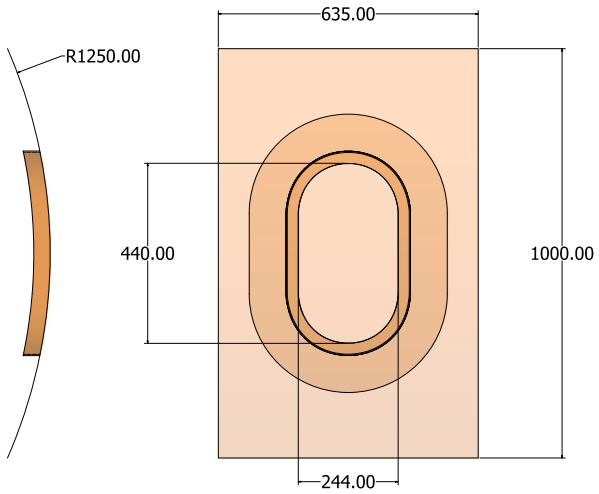

Fig. 12. Detailed level window drawing design dimensions (mm) [6].

Table 8
Detail level model passenger window information.

Model	Bird	Window Frame	Window Pane	Fuselage Skin
Shell Thickness (mm)	–	3	9.6	2.5
Material	Gelatin	Al 7050-T7451	Polycarbonate	Al 2024-T42
Mesh element Type	- Explicit, Linear - C3D8R - Conversion to Particles: On - Time based criterion - Time threshold: 0	- Explicit, Linear - S4R - Reduced Integration: On - Element Deletion: On	- Explicit, Linear - S4R - Reduced Integration: On - Element Deletion: On	- Explicit, Linear - S4R - Reduced Integration: On - Element Deletion: On
Element Global Size (m)	0.004	0.0045	0.005	0.007

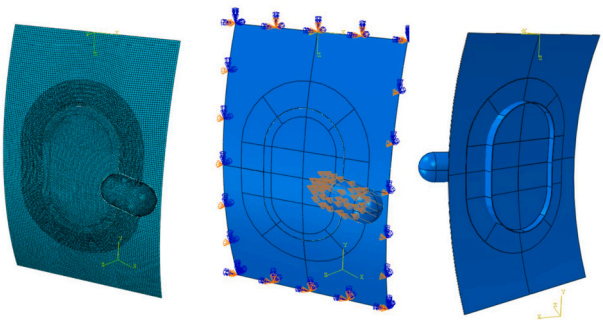

Fig. 13. Detailed Level, meshed model and boundary conditions.

passenger window dimensions are in between the size of the Airbus A350 and Boeing 787 passenger windows. The summary of the window model created in Abaqus is shown in Table 8.

The rear model meshed view, and its boundary conditions are shown in Fig. 13. The top and bottom edges of the fuselage skin are clamped, and the side edges are defined as symmetric. A velocity of 70 m/s is assigned to the bird model, and the window assembly is rotated 63.5 degrees with respect to the bird's flying direction.

2.4.4. Sub-component level

Two window sections are used at the sub-component level. The model is expanded from the detailed model by adding a pane clamp, clamp fastener, stringers, fuselage frames, and point-based fasteners. The model information is shown in Table 9.

Reduced integration is turned off at this level to generate more accurate results. The dimensions used for the fuselage frames and stringers are referenced from the configuration of the Convair 880 [18]. The exploded view of the sub-component is shown in Fig. 14.

Table 9
Sub-component level passenger window model information.

Model	Shell Thickness	Material	Mesh element Type	Element Global Size (m)
Bird	–	Gelatin	Explicit, Linear C3D8R Conversion to Particles: On Time based criterion Time threshold: 0	0.0045
Window Frame	3 mm	Al 7050-T7451	Dynamic explicit Linear S4R Reduced integration: Off Element Deletion: On	0.006
Window Pane	9.6 mm	Polycarbonate		0.0055
Fuselage Skin	2.5 mm	Al 2024-T42		0.0065
Pane Clamp	3 mm	Al 7050-T7451		0.0055
Clamp Fastener	2 mm	Al 7050-T7451		0.005
Stringer	2.5 mm	Al 2024-T42		0.025
Fuselage Frame	2.5 mm	Al 2024-T42		0.01
Fuselage Shear Clips	2.5 mm	Al 2024-T42		0.005

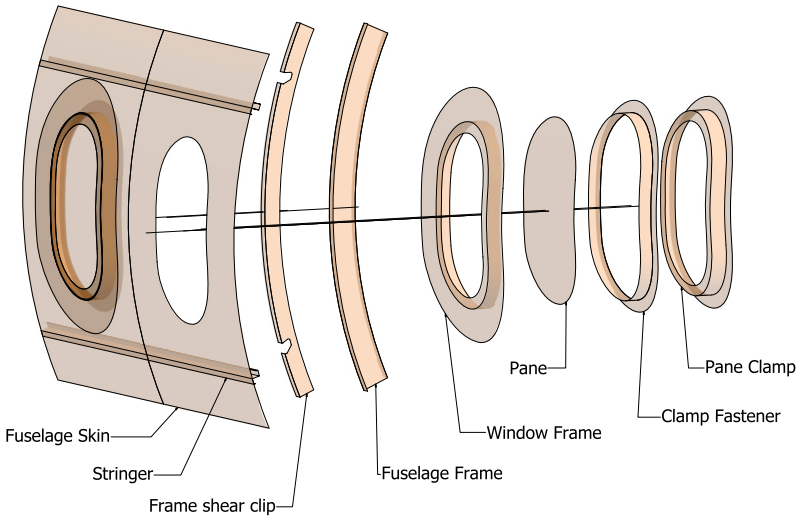

Fig. 14. Sub-component level surface model exploded view. [6].

Table 10
Point-based fastener distance in Abaqus model.

	Metal (m)
Edge distance	0.02
Pitch	0.04
Fastener spacing	0.05

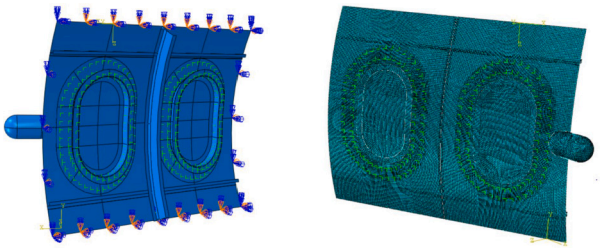

Fig. 15. Sub-component, meshed model and boundary conditions.

Tie constraints combine the two fuselage skin sections, stringers to the fuselage skin, frame clips to the fuselage skin, and frame to the frame clips. The passenger window structure components are attached by point-based fasteners 10 mm in diameter. Double-rowed fasteners attach the skin and window frame to allow a stiffer bonding between the impacted structure. The fastener mounting parameters are shown in Table 10 by applying guidelines provided by Fokker Aerostructures. The model constructed in Abaqus is shown in Fig. 15. The boundary conditions are identical to the detailed model. The bird impact velocity remains at 70 m/s with an impact angle of 63.5 degrees, representing the leading edge's Flying-V sweep angle.

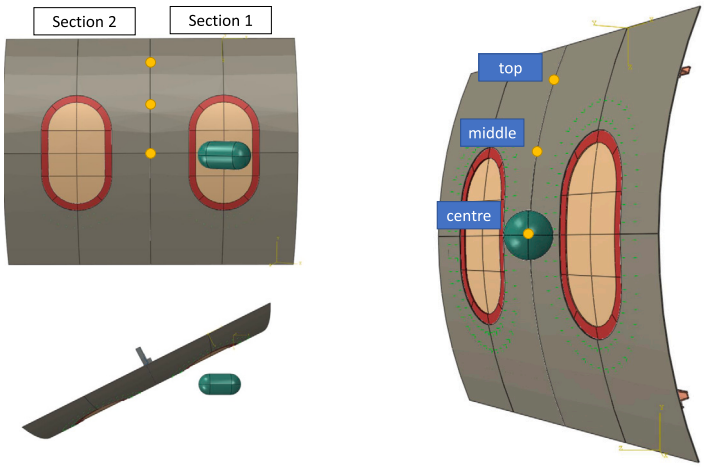

Fig. 16. Fuselage frame three impact location study.

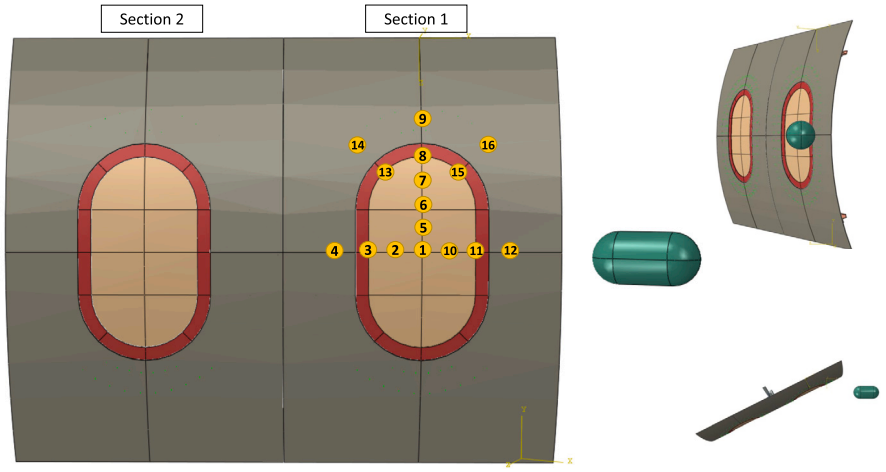

Fig. 17. Passenger window 16 impact location study.

Critical locations of the bird strike on the Flying-V fuselage and passenger window are determined at this level. The goal is to determine the impact location that generates the highest amount of plastic deformation, measured by the amount of plastic energy absorbed by the structures during the bird strike. With the critical region for plastic deformation determined, it is possible to facilitate the design of structures that prevent the structure from achieving plastic deformation. The two critical impact locations herein studied are the skin at the fuselage frame shear clip and the passenger window. Since the model is symmetric along the horizontal centre line, the impact points above the centre line can represent the impact behaviours described below. Three impact locations are planned for the fuselage frame impact, as depicted in Fig. 16.

For the window, 16 impact locations are planned, as shown in Fig. 17. It is intuitive to think that the impact locations near the clamped and symmetric boundary regions where the fuselage frames and stringer are located have a lower plastic strain. To find the weakest impact spot, using a three-bay model will only increase computational time and will unlikely change the fact that the weakest impact spot is close to the passenger window. Therefore, a two-bay model is sufficient to generate reliable results to meet the goal at the sub-component level.

Impact locations 3, 8, 11, 13, and 15 are the pane and window frame boundaries. Impact locations 4, 9, 12, 14, and 16 are the fuselage skin section stiffened by the window frame behind them.

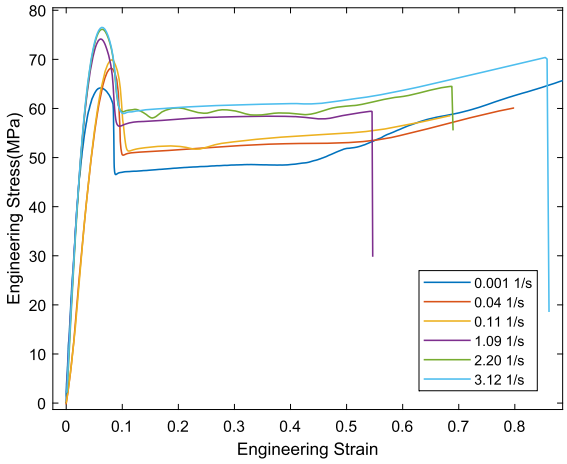

Fig. 18. Experimental nominal stress-strain curves for different loading rates.

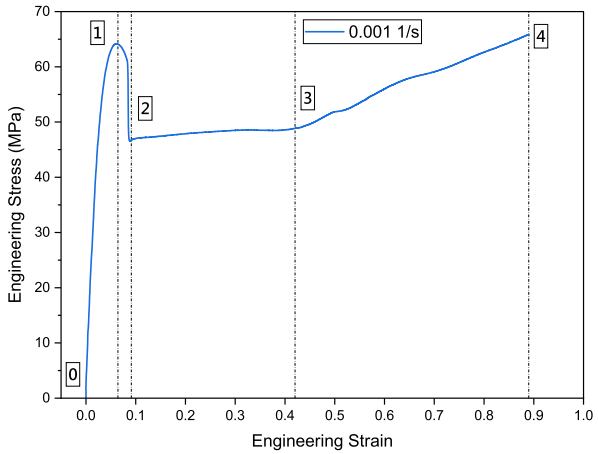

Fig. 19. Experimental nominal stress-strain curve and its necking phenomenon at 0.001 s^{-1} tensile strain rate.

Table 11
Young's modulus and the mean value for 6 mm/min loading rate.

Specimen Number	1	2	3	4	5	mean	STD
Young's Modulus (GPa)	2.0389	2.1257	2.1462	2.9143	1.6321	2.1714	0.465

3. Results and discussion

3.1. Coupon level

3.1.1. Polycarbonate material characterisation

The nominal and true stress-strain data of different loading rates are compared by selecting the first specimen of the same loading rate samples shown in Fig. 18. The four stages of the engineering stress-strain curve are explained by using the 6 mm/min (0.001 s^{-1}) loading rate coupon shown in Fig. 19.

The first stage (0-1) is the elastic region of the polycarbonate. The stress is proportional to strain, and its deformation is reversible. The slope of the linear behaviour is Young's modulus. Young's modulus is determined by performing a first-order polynomial fit of a range of stress-strain data points. Since the ASTM D638 did not specify a range, the standard from ISO 527 (Plastics — Determination of tensile properties) is used for reference. The range of the data is defined as the strain interval between 0.05% and 0.25%. The 6 mm/min loading rate is used to determine Young's modulus of the polycarbonate since the extensometer can only be attached to low loading rates. An extensometer is recommended to measure Young's modulus by the ASTM D638. The Young's modulus of the five specimens and the mean value at a 6 mm/min loading rate are shown in Table 11.

The tensile strength at yield is the point at the end of the stress-strain curve and the start of the plasticity. Yield strength is the maximum tensile strength (nominal) sustained during the tensile test determined from Fig. 18. The mean maximum tensile strength for each loading rate is shown in Table 12.

Table 12
Experimental mean tensile strength at yield.

Loading Rate (mm/min)	6	300	750	7500	15000	30000
Mean Tensile Strength at Yield (MPa)	64.146	68.728	69.924	74.303	76.459	76.945
STD	0.263	0.440	0.150	0.234	0.464	0.618

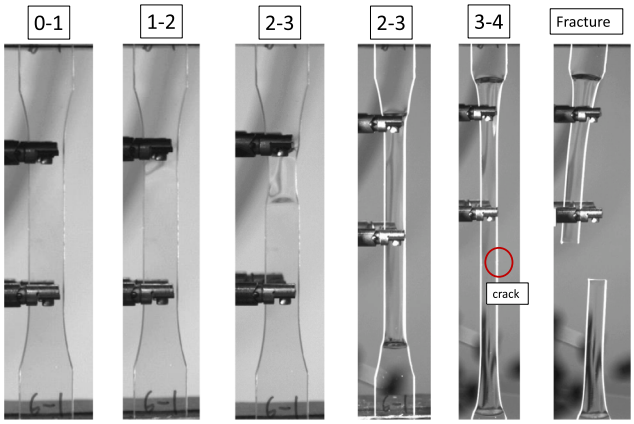

Fig. 20. Tensile test elongation history for the first coupon at 6 mm/min loading rate. The number blocks are the stages shown in Fig. 19.

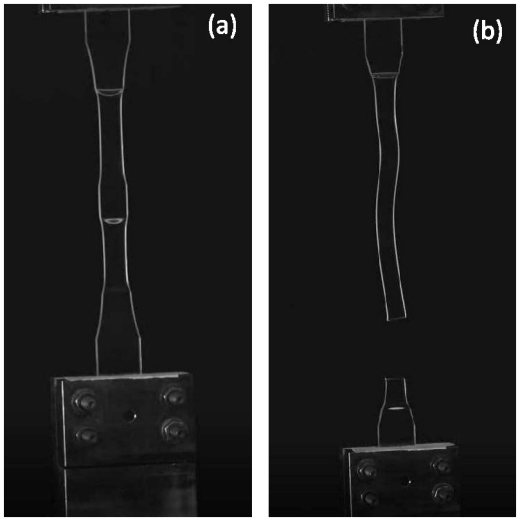

Fig. 21. (a) At a 7500 mm/min loading rate, two location necking occurs. (b) At a 30000 mm/min loading rate, the coupon's wave-shaped deformation after fracturing.

After the yield strength, strain softening, a phenomenon in which stress decreases with increasing strain, occurred in the second stage (1-2). Necking occurs at this stage, exerting a local stress concentration in the narrow section of the coupon. The necking phenomenon continues as a stable necking or an unstable necking. Both stable and unstable necking leads to the third stage (2-3), where a constant stress plateau is formed, and the necking region increases in the coupon. Small cracks are generated at the third stage for coupons having unstable necking, which leads to an early fracture. Coupons with stable necking progress to the fourth stage (3-4), where strain hardening occurs. The stress increases with the increasing strain due to the amorphous polymer orientation of the polycarbonate material. The increasing stress concentration at this stage caused generating cracks that eventually led to failure. Fig. 19 shows a stable necking that fails at the strain-hardening phase. Its tensile test elongation history is demonstrated in Fig. 20. It is observed that double necking can happen at stage 3 (2-3) which the first coupon at a loading rate of 7500 mm/min is shown in Fig. 21 (a) as an example.

The nominal failure strain determined from Fig. 18 is defined as the strain at the rupture point. The mean values for each loading rate are shown in Table 13. The fracture strain mean values are used in the simulation model to consider that the cracks in different coupons are generated at different stages and times. Some coupons with low fracture strains might be due to the slight edge defects at the narrow section generated during the water jet cutting of the coupons. For a fracture at a higher tensile loading rate of 30000 mm/min, the reaction stresses generated upon fracture propagate back to the specimen, causing the wave-like deformation shown in Fig. 21 (b).

Table 13
Experimental mean nominal failure strain.

Loading Rate (mm/min)	6	300	750	7500	15000	30000
Mean Nominal Failure Strain (%)	87.6177	76.4842	72.2048	64.1896	66.0747	75.8940
STD	0.031	0.044	0.074	0.135	0.041	0.144

Table 14
The corresponding mean strain rate of the loading rates.

Loading Rate (mm/min)	6	300	750	7500	15000	30000
Strain Rate (%)	0.0009	0.0432	0.1058	1.0897	2.2015	3.1207
STD	4E-06	3E-04	9E-04	1E-03	2E-03	5E-02

Table 15
Mean Young's modulus for different strain rates.

Loading Rate (mm/min)	6	300	750	7500	15000	30000
Mean Young's modulus (GPa)	2.1714	0.7056	0.7835	2.2869	2.3701	2.4597
STD	0.465	0.095	0.075	0.015	0.035	0.011

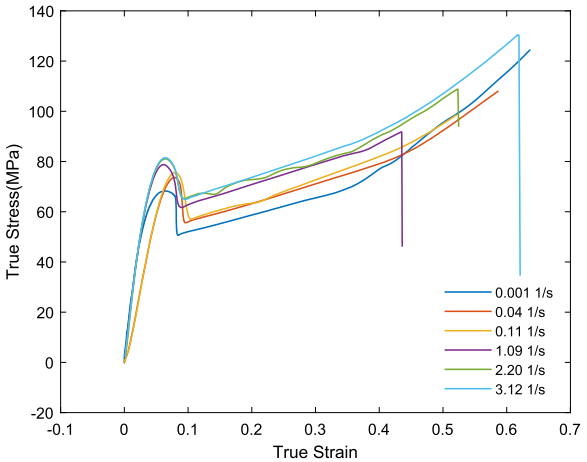

Fig. 22. Experimental true stress-strain curve for different loading rates.

The strain rate is determined by performing a first-order polynomial fit of the strain-time data point generated by the data logging. The slope is defined as the strain rate. The mean values of the strain rates for the corresponding loading rates are shown in Table 14.

There are discrepancies in Fig. 18 that strain rates at 0.04 and 0.11 s^{-1} have lower slopes than the other strain rates. The discrepancies are due to the different displacement measurement methods used for the 0.04 and 0.11 s^{-1} strain rates. A lower Young's modulus is obtained using the machine's displacement data and the 115-mm initial length. The 0.001 s^{-1} strain rate that uses the extensometer displacement data and the 50-mm initial length gives Young's modulus that conforms closer to the material data sheet. The higher strain rates tested with the MTS machine have similar slope values with the result of the 0.001 s^{-1} strain rate. Table 15 shows that the mean Young's modules for the strain rates at 0.001, 1.09, 2,20 and 3.12 s^{-1} conforms to the results by Fu et al., Cao et al. Kendall et al. and Xu et al. [11,5,16,29] which Young's modulus has a slight increase when the strain rate increases. The Young's modulus used in the simulation is the 0.001 s^{-1} strain rate value. The plasticity ad failure properties of strain rates at 0.04 and 0.11 s^{-1} are still implemented in the simulation since it gives a more conservative result. The phenomenon of yield stress increases with the increased load rate for all the tested loading rates conforms to the literature results [11,5,16,29].

The true stress-strain curves are shown in Fig. 22. The simulation model will use its plasticity behaviour after the yield point.

3.1.2. Polycarbonate numerical model behaviour

The material behaviours specified in the material model are elastic, plastic, ductile damage, and density. The Young's modulus is determined from the mean value of the 0.001 s^{-1} strain rate shown in Table 11. The fracture strain of the ductile damage is the average fracture strain of each strain rate. Using the average value can take the fracture from the unstable necking into account. Since the interested polycarbonate behaviour in this study is the elastic-plastic transformation region. The accuracy of the fracture strain does not contribute much to the outcome. The plastic stress-strain behaviour of each strain rate is loaded in the model for the plastic behaviour. The first plasticity data point of each strain rate in Abaqus has to start with a plastic strain of 0, and the corresponding true stress is the true yield stress. The true stress and the plastic strain are determined using Equation (3) and Equation (4). It is defined in ISO 527 at the data point that the tangent slope in the true stress-strain curve equals zero. For simplicity, the maximum

Table 16
True yield stress and yield strain.

Strain Rate (s^{-1})	0.001	0.04	0.11	1.09	2.20	3.12
True Yield Stress (MPa)	68.257	73.669	75.622	78.765	81.095	81.503
True Yield Strain	0.0641	0.0782	0.0795	0.0611	0.0651	0.0641

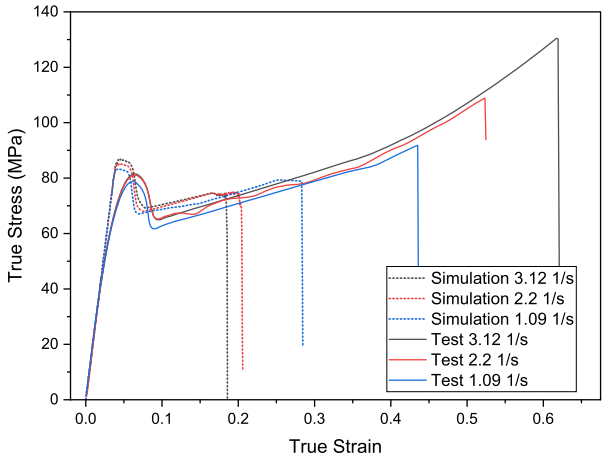

Fig. 23. True stress-strain compared with Abaqus dynamic explicit simulation.

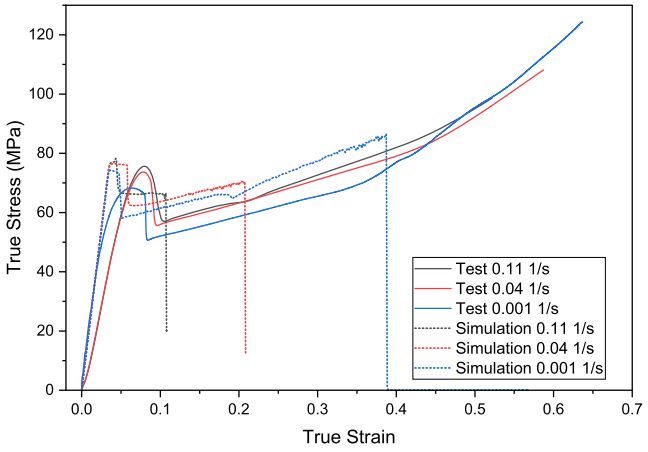

Fig. 24. True stress-strain compared with Abaqus dynamic explicit simulation.

true stress at the elastic-plastic transfer's true strain range is determined for the stress of zero plastic strain. The true yield stress and its corresponding true strain are given in Table 16.

The comparison of simulation with testings at each strain rate is shown in Fig. 23 and Fig. 24.

The linear slope up to the yield point before strain softening is Young's modulus of the 0.001 s^{-1} strain rate defined as the model's elastic property. The model can capture the strain rate-dependent yield stress, strain softening after yield, and the strain hardening effect till fracture. The available material behaviours defined in the model do not capture the strain softening before the yield point, which leads to higher yield stress and stress at the plasticity region. The Mises stress and the equivalent plastic strain (PEEQ) history of the 3.12 s^{-1} is shown in Fig. 25. The model can demonstrate the stability of the double-necking phenomena in Fig. 26.

The strain at failure is an apparent discrepancy between the simulation and the testing result, resulting in a toughness difference. In Abaqus, an energy type damage evolution is selected and is specified as the fracture energy obtained from the polycarbonate material data sheet. The value from the material data sheet may be too low for tensile testing since the fracture energy is determined by the Izod notched impact test with a pre-notch. Since there are no pre-cracks during the tensile tests herein, the damage evolution value should be increased in Abaqus to match the results of the tensile tests. The authors adopted the data sheet value for the forthcoming bird strike simulations due to the need for experimental data obtained with compatible strain rates.

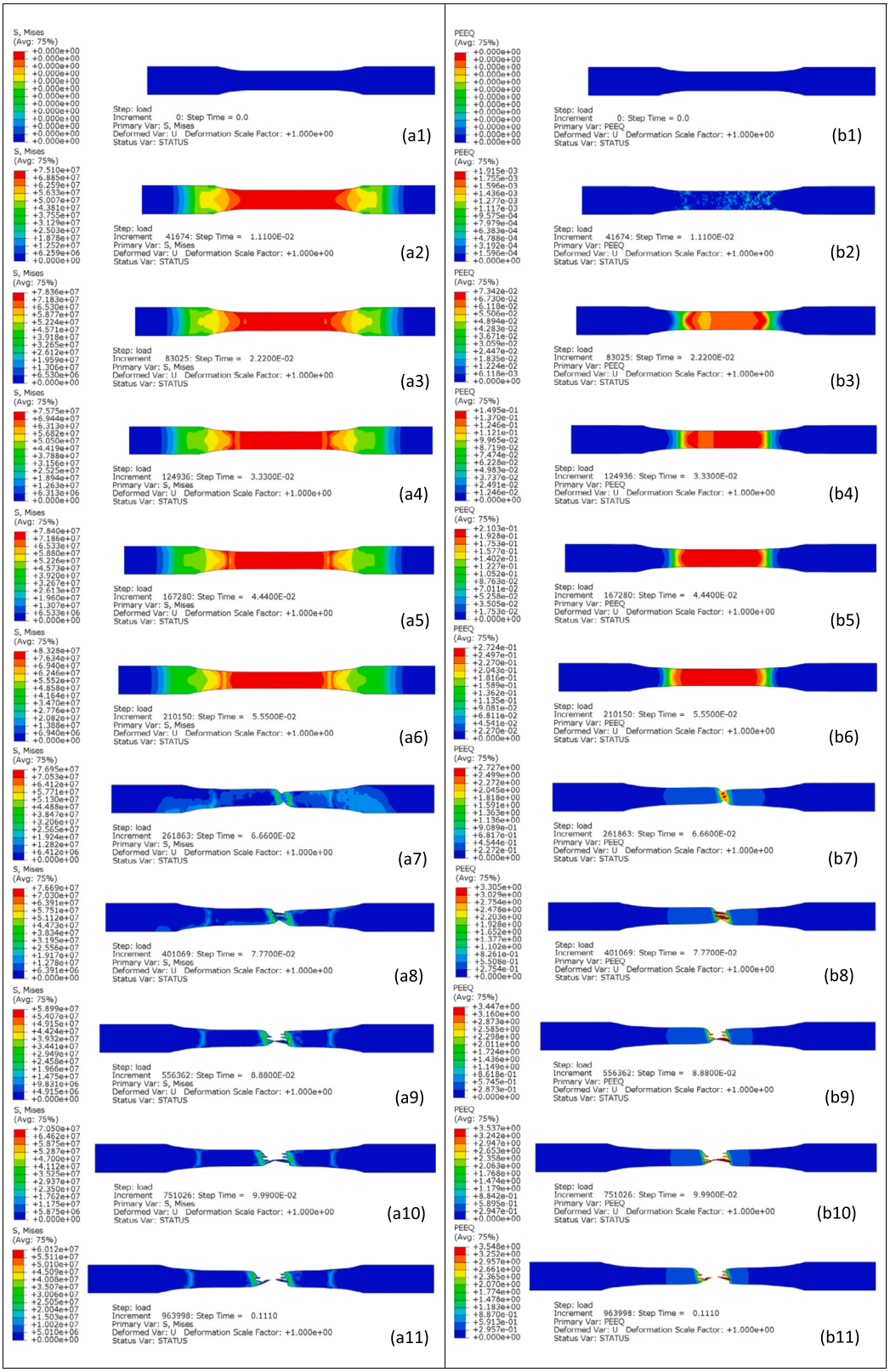

Fig. 25. Abaqus dynamic explicit simulation tensile history at 3.12 s^{-1} strain rate. (a1) to (a11) shows the Mises stress distribution with an 11.1 ms interval. (b1) to (b11) shows the equivalent plastic strain distribution with an 11.1 ms interval.

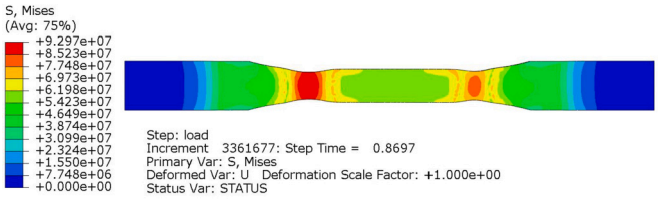

Fig. 26. Double necking behaviour at 0.11 $s^{-}1$ strain rate.

3.1.3. Improving polycarbonate's testing process

The polycarbonate testing process was conducted first using the ZwickRoell machine for low loading rates up to the maximum of 750 mm/min. Afterwards, the MTS machine was used for higher strain rates at 1.09, 2.20 and 3.12 s^{-1}. The results of the stress-strain curves derived in Fig. 18 and Fig. 22 showed that the MTS machine-generated data for calculating Young's moduli conform with the modulus of elasticity determined by the ZwickRoell machine with an extensometer. Since the MTS machine can also perform quasi-static loading rates, it should be used to perform all tensile test speeds for future testing scenarios. However, using the MTS machine to perform all test speeds is not capable due to the limitation of the MTS extensometer's (model 634.11F-2x) strain limit. Once the strain limit is reached, the tensile test is halted to remove the extensometer, while the ZwickRoell machine with an extensometer attached does not have this issue. The temporary halt of the tensile test may generate undesired and unexpected test results for dynamic test cases. Therefore, the test process can be improved for standardisation by conducting the 6 mm/min using the ZwickRoell machine to determine Young's modulus, which follows the ASTM D638 requirements. Afterwards, complete the rest of the higher loading rates using the MTS machine.

3.1.4. Bird material behaviour

The 70 m/s speed impact history for the 25-mm thick aluminium 2024-T42 normal and inclined plate is shown in Fig. 27. From the impact sequence results, information that can be obtained are:

- A 25-mm thick aluminium 2024-T42 plate has no plasticity generated during the impact history. The thickness can be used as a thick plate for bird material study.
- The maximum stress location changes over time in the plate for the inclined impact. Therefore, the maximum Mises stress of the impact history is recorded at different locations. An element set excluding the elements near the edges is created in both the normal and inclined model to record the Mises stress of the elements' integration points during impact. The maximum stress value at each time interval is plotted as the Maximum Mises stress history envelope.
- For an inclined impact, the surroundings of the hemispherical-ended bird have the first contact with the plate. Not the centre of the dome.

The maximum Mises stress history envelops are shown in Fig. 28, and the ALLIE histories are shown in Fig. 29. The horizontal axis is the impact time, in which the theoretical impact duration t_D of the normal and inclined impacts are marked as dotted lines.

The theoretical duration of impact t_D is determined by using Equation (10).

$$t_D = \frac{L}{u_0} \tag{10}$$

The duration of impact is the estimated time for the travel of its full length L with an initial velocity of u_0. L for the bird is 0.2268 m and for a 70 m/s impact U_0 is 70 m/s. Thus the duration of impact for the 4 lb bird at 70 m/s is shown in Equation (11):

$$t_{D,70} = 0.0032 \tag{11}$$

The stress and energy values after the impact duration are the response of the plate after impact. The normal impact generated higher peak stresses and impact energies than the inclined impact. Before the impact duration, the peak stress and energy and their corresponding time can be used as characterisation parameters for different bird materials. The simulation results can then be compared with the measurements of strain gauges and pressure sensors. The deformation history can be compared with a high-speed camera.

3.2. Element level

The Mises stress distribution histories for the three different plate materials of the inclined and normal impact are shown in Fig. 30.

The Mises stress history of the 70 m/s speed at inclined impact for the three materials is shown in Fig. 31.

From the impact sequence results, information that can be obtained are:

- Stress waves are created and propagated in the plate during impact. Polycarbonate material has a more concentrated stress distribution than aluminium.

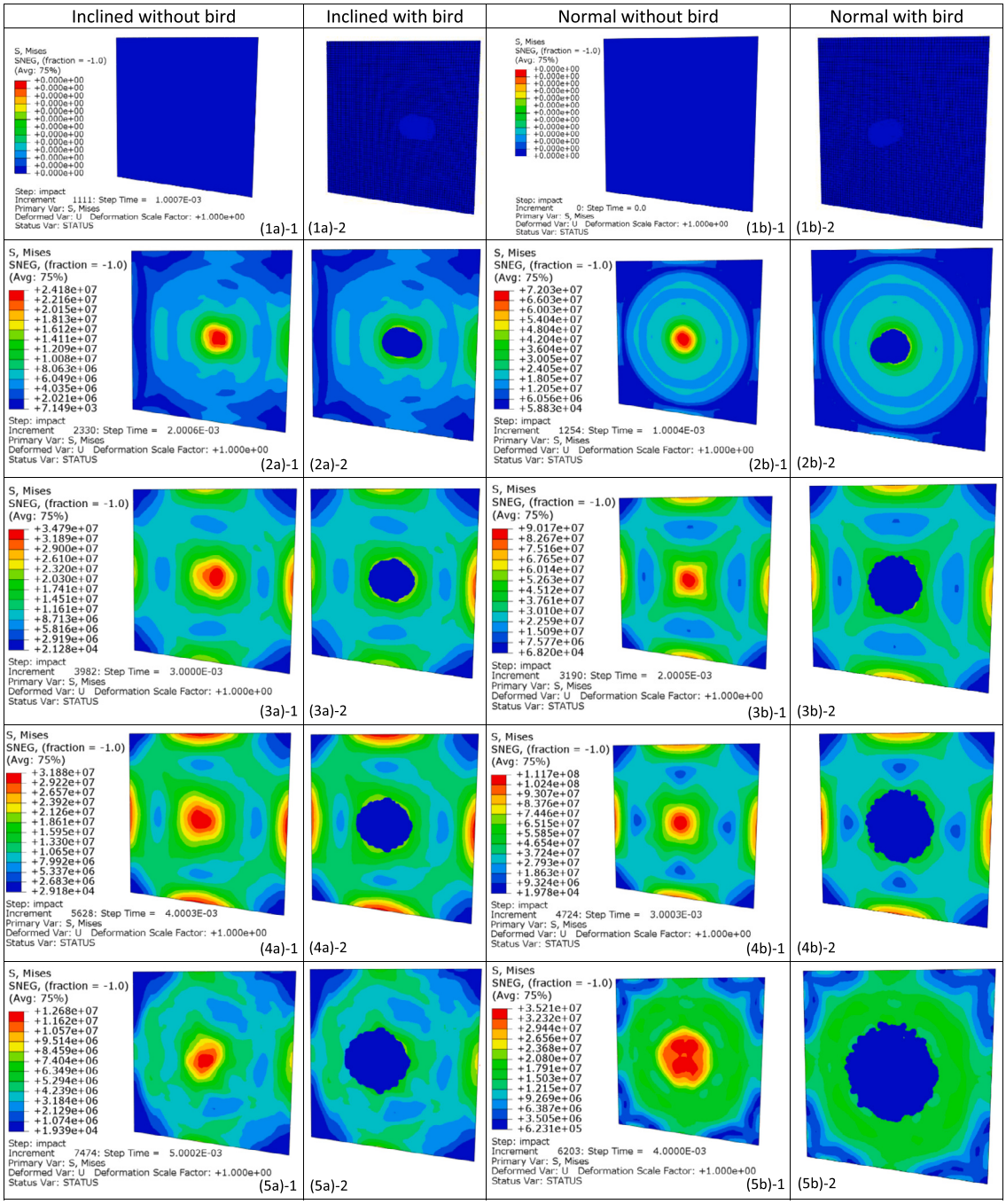

Fig. 27. Mises stress behaviour of a 70 m/s bird impact on normal and inclined 25-mm thick aluminium 2024-T42 plates. (1a) to (5a) shows the inclined impact history of the bird. (1b) to (5b) shows the normal impact history of the bird."-1" is the impact history with the bird hidden, and "-2" is the impact history with the behaviour of the bird. 1-ms time interval is shown for each frame.

- The inclined impact exerts less stress on the plate due to a lower velocity component normal to the plate. In addition, the Flying-V has a sweep angle of 63.5 degrees, larger than most commercial aircraft, which usually have a sweep angle below 40 degrees. Therefore, the Flying-V has less damage to the wing-fuselage leading edge when compared to the leading edge of a conventional aircraft wing.
- For the inclined impact, a high-stress region in front of the bird impact direction occurred due to the squeezing effect of the bird and plate material.

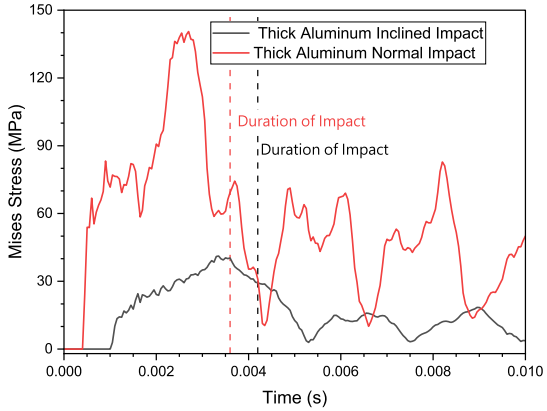

Fig. 28. Maximum Mises stress histories of the 25-mm thick aluminium 2024-T42 plate.

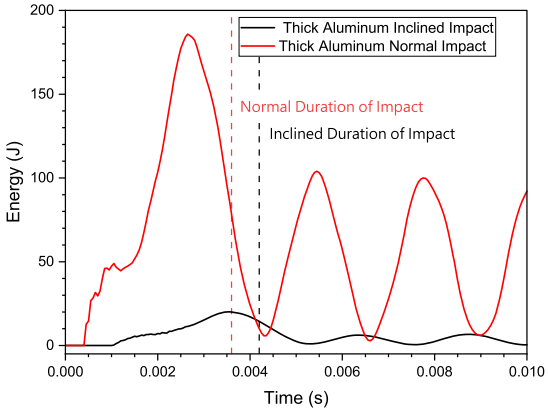

Fig. 29. ALLIE of the 25-mm thick aluminium 2024-T42 plate.

The internal energy (ALLIE) history for the three different plate materials of the inclined and normal impact are shown in Fig. 32 and Fig. 33. The Maximum Mises stress history for the three different plate materials of the inclined and normal impact are shown in Fig. 34 and Fig. 35. The Plastic dissipated energy (ALLPD) histories for the three different plate materials of the inclined and normal impact are shown in Fig. 36 and Fig. 37. The dotted lines are the impact duration for the normal and inclined impact.

Polycarbonate has the best energy absorbance ability, more than two times compared to the aluminium 7050-T7451 and the 2024-T42, which have similar ALLIE. However, polycarbonate generates the highest plasticity in an inclined impact due to having the lowest yield stress. Aluminium plates have higher peak stress than polycarbonate plates since they have a higher modulus of elasticity. While the peak stress occurred at the moment of contact, the ALLIE and ALLPD peaked after the impact duration when the stress waves propagated throughout the flat plate. The plasticity generated by the inclined impact is 20 times less for polycarbonate and 140 times less for aluminium 2024-T42. The 63.5-degree Flying-V sweep angle gives the advantage of reducing bird strike. While the thickness increment of the polycarbonate to 9.6-mm can zero the plasticity at the inclined impact shown in Fig. 38, the thickness increment of the aluminium 2024-T42 above 3 mm will result in overweight for the fuselage skin and other structural components due to its higher density. Therefore, local thickness increments around the critical location of the window and using geometry change to stiffen the structure will be performed at the detailed level.

3.3. Detail level

The purpose of the detail level is to construct a rudimentary model for the bird strike simulation. The elastic strain (ALLSE) and the plastic strain (ALLPD) history is presented to compare the amount of energy absorbed in the structural component, shown in Fig. 39 and Fig. 40. The history of the bird strike stress distribution is demonstrated in Fig. 41.

Plastic strain is generated in the window frame and fuselage skin. The plastic strain in the pane is at the scale of 10^{-3}, which can be ignored, while the highest plastic strain is generated in the window frame. There are two phases of peaks in the ALLSE history: the first peak is at the time the bird impacts the windowpane at its duration of impact, and the second peak is when the bird slides along the windowpane and impacts the window frame and skin. Since the frame has a higher thickness and stiffener geometry, it deforms less, resulting in a lower ALLSE peak. After 14 ms, the bird material has no contact with the structure, and the stored elastic energy is released with some residual elastic energy. The limitation in the detailed level that prevents it from generating reliable

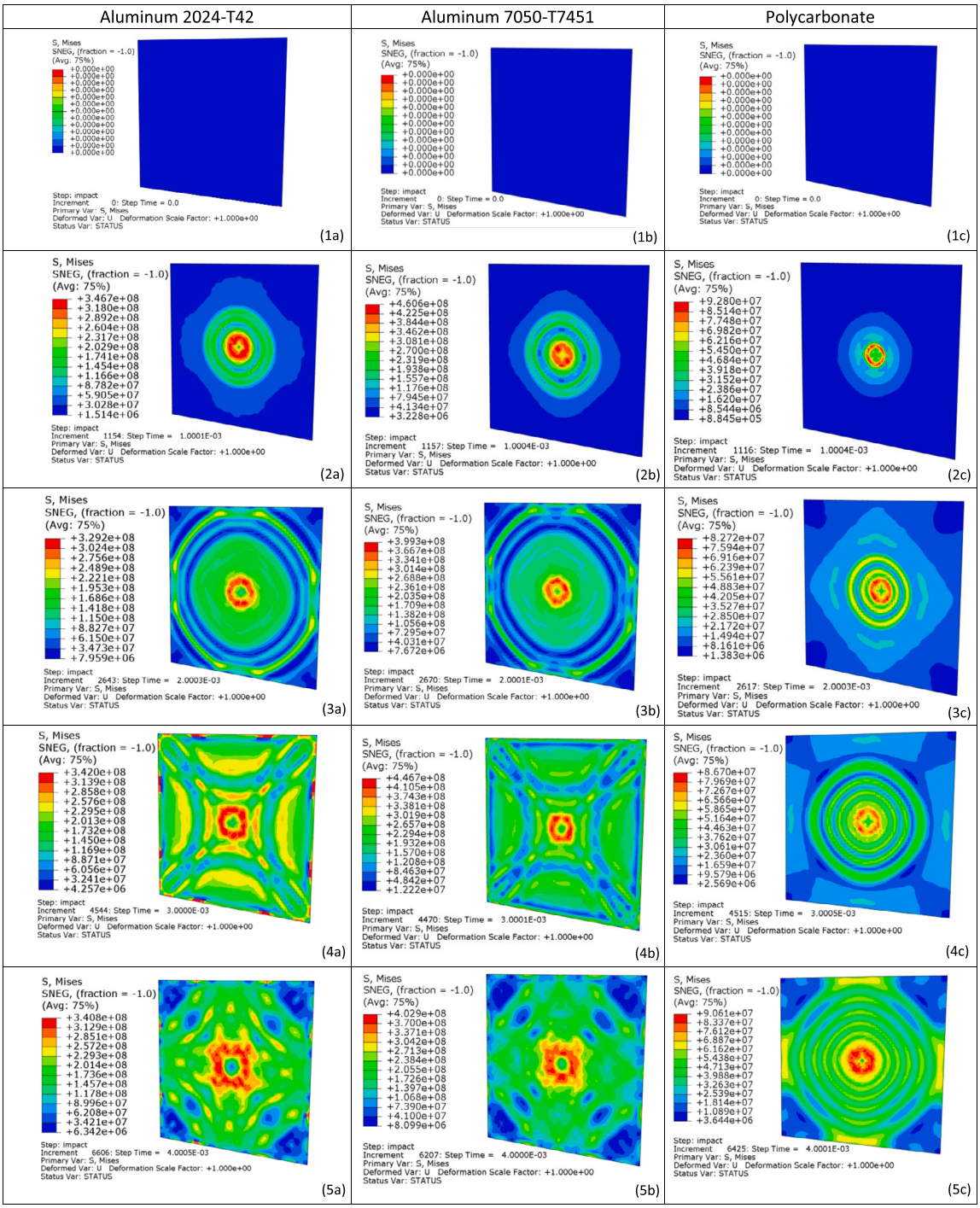

Fig. 30. Mises stress behaviour of a 70 m/s bird impact on a normal 3-mm thick plate. (1a) to (5a) shows the aluminium 2024-T42 impact history. (1b) to (5b) shows the aluminium 7050-T7451 impact history. (1 c) to (5 c) shows the polycarbonate impact history. 1-ms time interval for each shown frame is shown.

data is the lack of stiffening members around the fuselage skin. Another limitation of the detailed model is the undetected behaviour of its vicinity window sections. In Fig. 41, after 14 ms, the bird material is supposed to move to the other window section creating new stresses and plastic strain distribution, but the adjacent window and fuselage structure are absent. Therefore, from the detailed level results, it is learned that a second window section should be added in the sub-component level model.

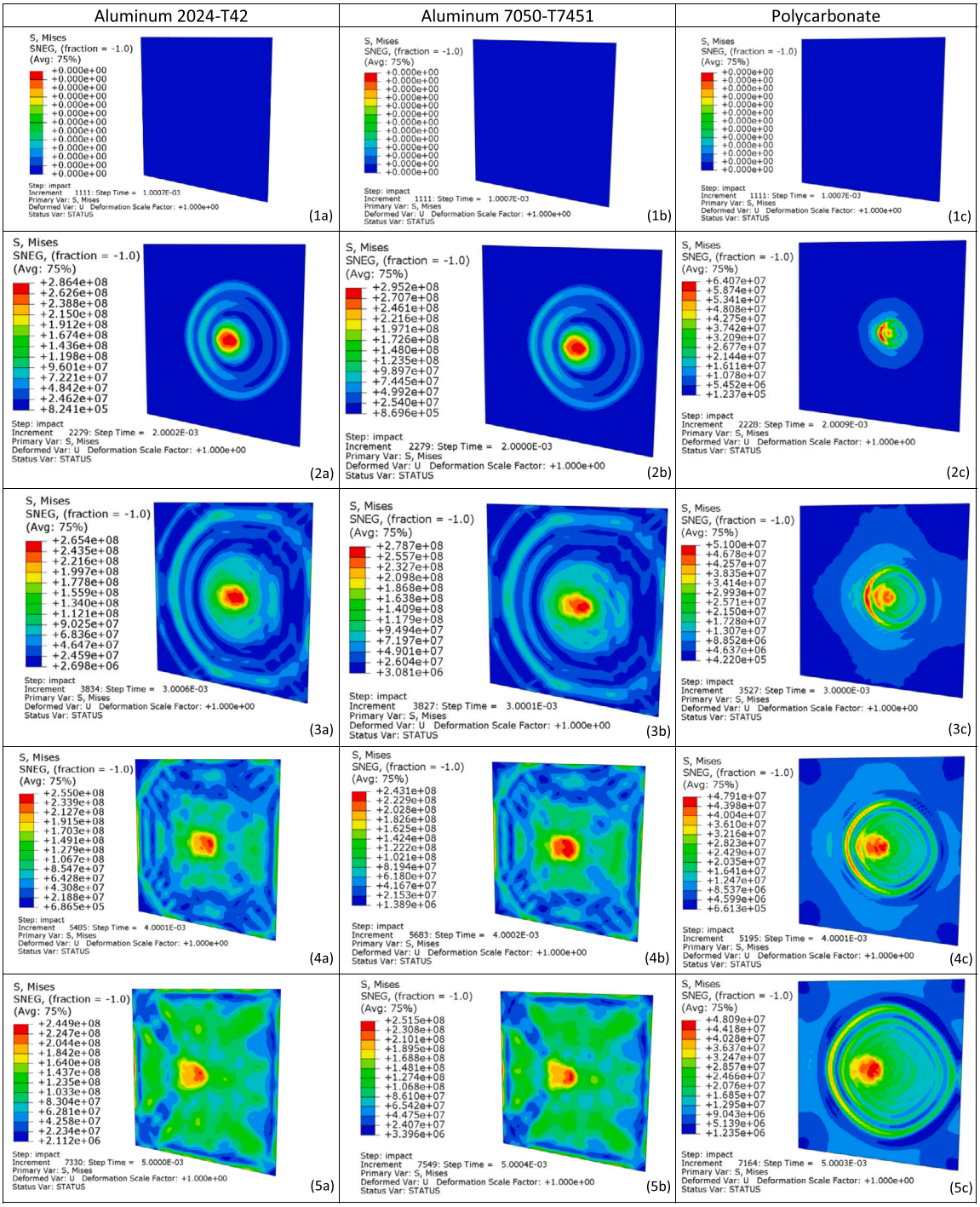

Fig. 31. Mises stress behaviour of a 70 m/s bird impact on a inclined 3-mm thick plate. (1a) to (5a) shows the aluminium 2024-T42 impact history. (1b) to (5b) shows the aluminium 7050-T7451 impact history. (1 c) to (5 c) shows the polycarbonate impact history. 1-ms time interval for each frame is shown.

3.4. Sub-component level

3.4.1. Fuselage frame impact

Fig. 42 and Fig. 43 show the fuselage frame's elastic and plastic energy impact history. Although the middle fuselage impact has the highest peak strain energy, it doesn't have the highest plastic energy. The highest plastic strain energy of 14 J occurs in the impact at the centre fuselage frame, while the top impact has the lowest plastic energy.

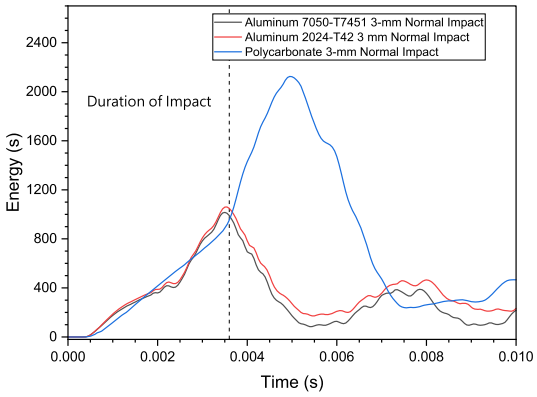

Fig. 32. ALLIE history of 3-mm thick flat plates normal-impacted by a 70 m/s bird.

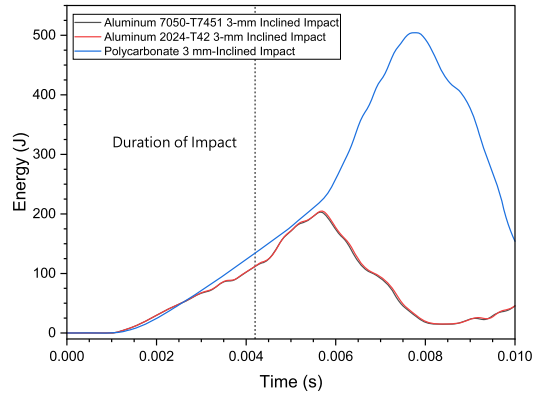

Fig. 33. ALLIE history of 3-mm thick flat plates incline-impacted by a 70 m/s bird.

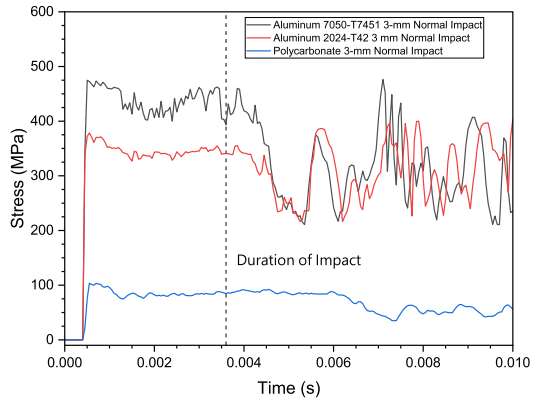

Fig. 34. Maximum Mises stress history envelop of 3-mm thick flat plates normal-impacted by a 70 m/s bird.

The plastic energy of the centre impact can be further inspected by its contributors in the window structure shown in Fig. 44. The main contributor is the fuselage skin in section 1 and the window frame in section 2. The contribution of the elastic strain is also shown in Fig. 45, where the fuselage skin (skin1/pink) has the highest contribution at the first peak and after the second peak.

The first peak is at the time of the bird's impact duration, and the second peak is at the bird having contact with the second window pane (pane2/green) and window frame (frame2/white). The energy peaks are illustrated with the motion of the bird materials and the Mises stress distribution from t = 0 ms to t = 18 ms shown in Fig. 46.

3.4.2. Passenger window impact

The location numbering of the window impact is shown in Fig. 17. The window impact location will be compared horizontally (1-4, 10-12), vertically (1, 5-9), and diagonally (13-16) by using the energy method.

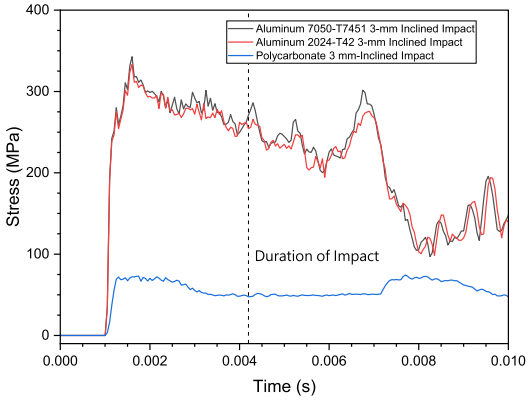

Fig. 35. Maximum Mises stress history envelop 3-mm thick flat plates incline-impacted by a 70 m/s bird.

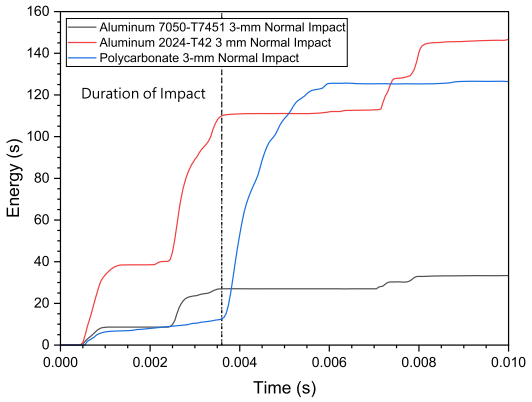

Fig. 36. ALLPD history of 3-mm thick flat plates normal-impacted by a 70 m/s bird.

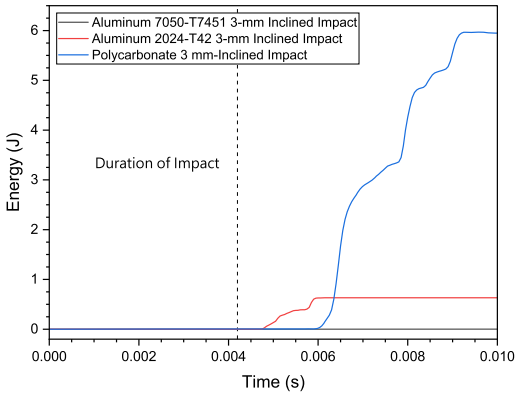

Fig. 37. ALLPD history of 3-mm thick flat plates incline-impacted by a 70 m/s bird.

For the horizontal impact, it is shown in Fig. 47 that the centre impact generates the highest amount of plastic energy. It also generates the highest peak of the internal energy shown in Fig. 48 since it is the location furthest away from the window frames. Impact location 2, 3, and 4 generates a lower amount of plastic energy than location 10, 11, and 12 since for 2, 3, and 4, the bird material slides to the stiffer skin-fuselage structure rather than 10, 11, 12, which the bird slides to the other side of the window frame and fuselage skin. To conclude, the critical location of the horizontal window impact is location 1.

For the vertical impact, location 6 is the most critical point that generates the highest plastic energy shown in Fig. 49. Starting from location 1 (centre of the window) and moving upwards, the generated plastic energy increases until it reaches location 7, closer to the window frame. Moving above location 7, the plastic strain generated will decrease since the bird material interacts less with the window structure. The internal energy ALLIE during the impact history is shown in Fig. 50. The window centre has the highest peak, although it doesn't have the highest ALLPD.

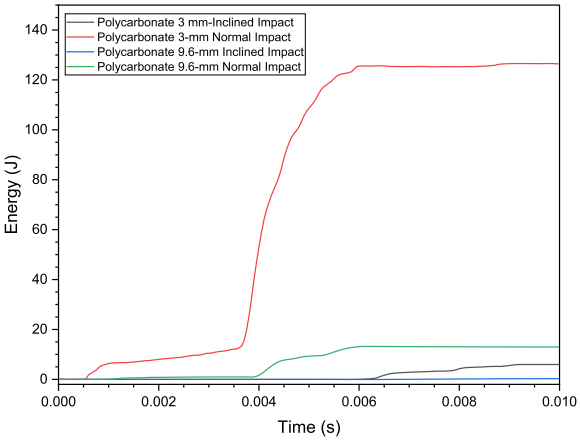

Fig. 38. ALLPD history of 3-mm thick flat plates incline-impacted by a 70 m/s bird.

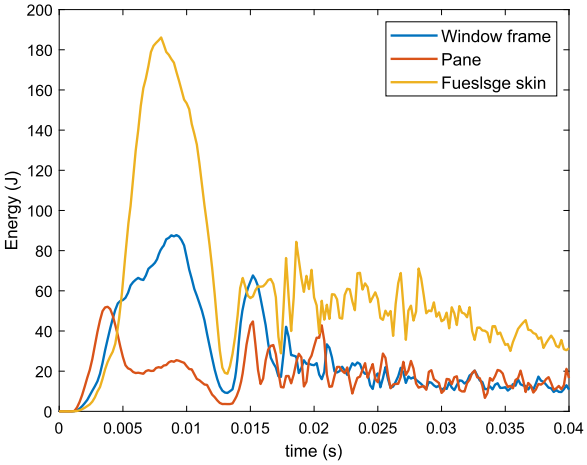

Fig. 39. ALLSE in the structure components.

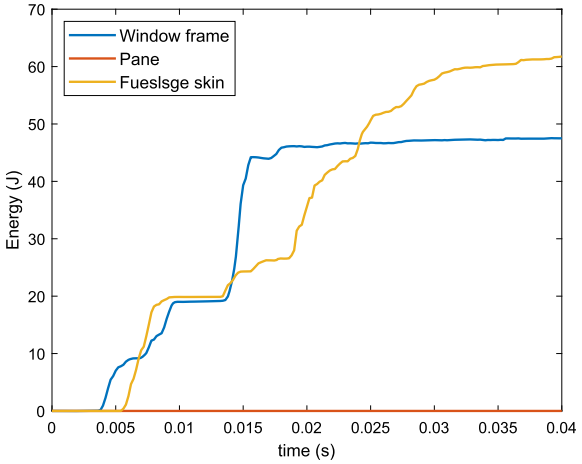

Fig. 40. ALLPD in the structure components.

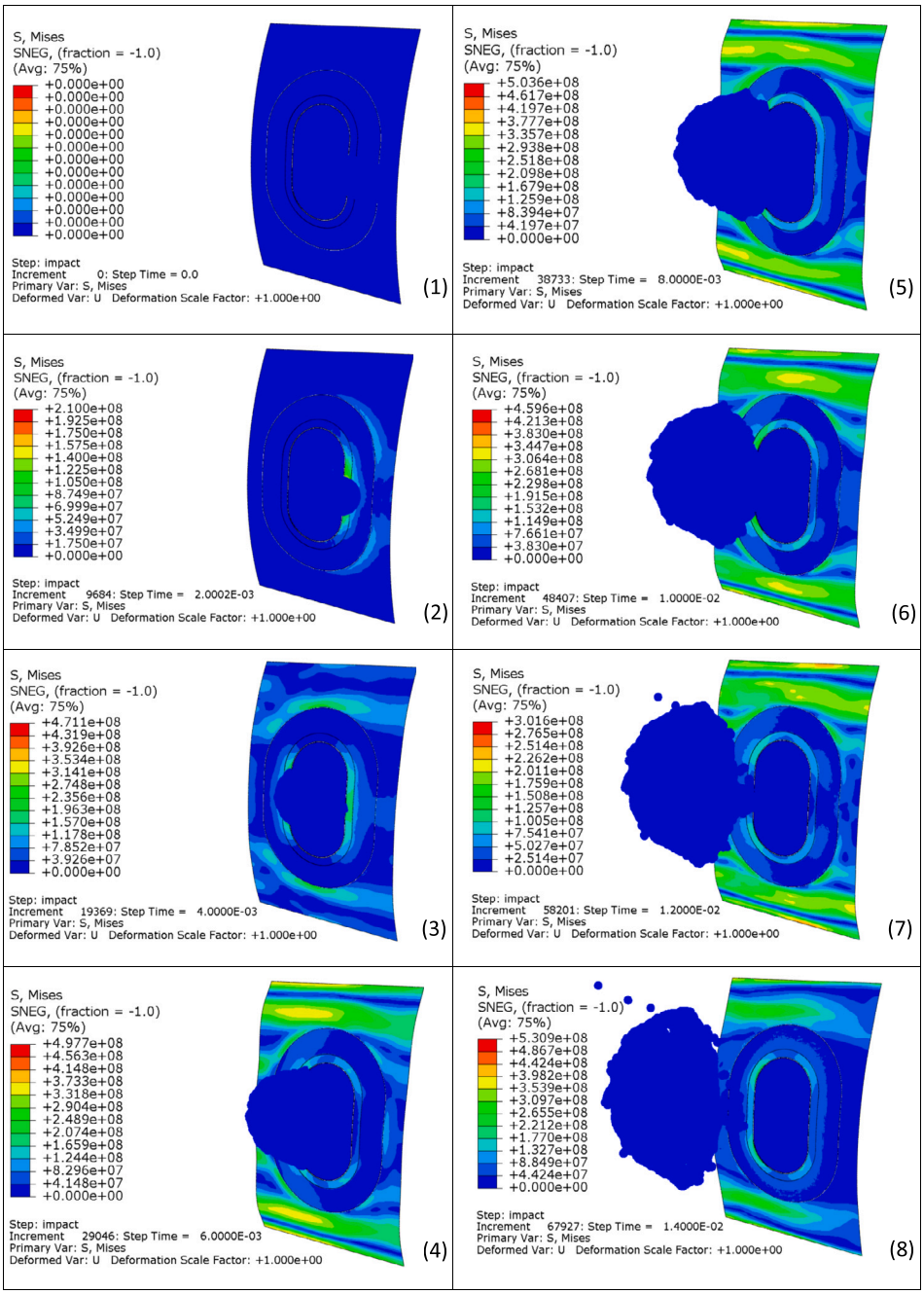

Fig. 41. Detailed level 70 m/s bird strike stress distribution. The frames (1) to (8) are the impact sequence with a 2 ms time interval.

For the diagonal impact, location 15 has the highest amount of plastic energy shown in Fig. 51. Location 15 generated more plastic energy than location 13, similar to the results in the horizontal impact in which the impact of the right half-side window has more damage than the left. The internal energy ALLIE is shown in Fig. 52.

It should be noted that locations 12 and 16 are not impacted at the location shown in Fig. 17 but at the updated location in Fig. 53. Switching locations 12 and 16 to section 2 is because the impacting location is too close to the skin panel boundary, which has no fuselage frame. The deformation of the skin panel and the window frame is too high that the bird will penetrate through the window. A more realistic approach would be impacting 12 and 16 at window section 2 so that there is support from the fuselage frame. A three-window section would be an ideal model, but studying various points would have a higher computational cost. Since the goal on this level is to search the critical point, it is intuitive to think that the impact locations near the clamped boundary regions where the fuselage frames and stringer are located have low ALLIE and ALLPD without extending the model size. Therefore, switching impact locations for 12 and 16 is performed.

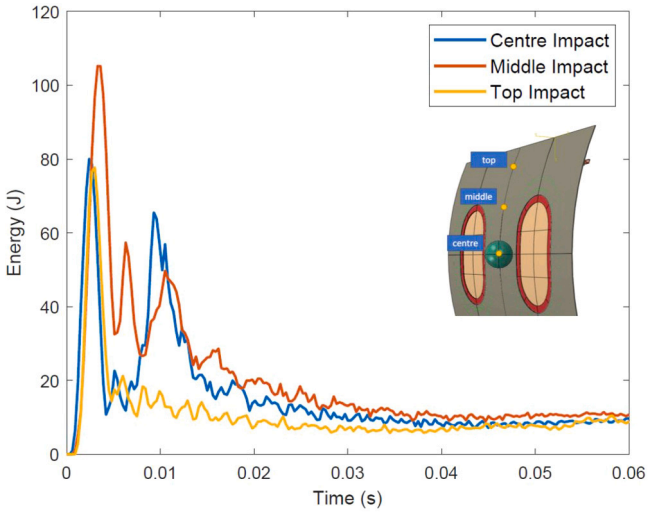

Fig. 42. Fuselage frame impact ALLSE comparison.

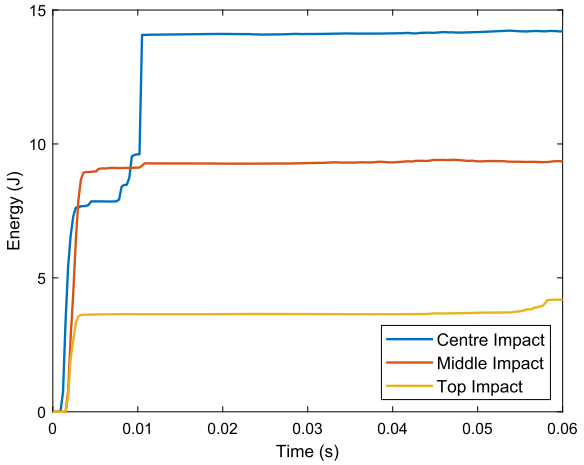

Fig. 43. Fuselage frame impact ALLPD comparison.

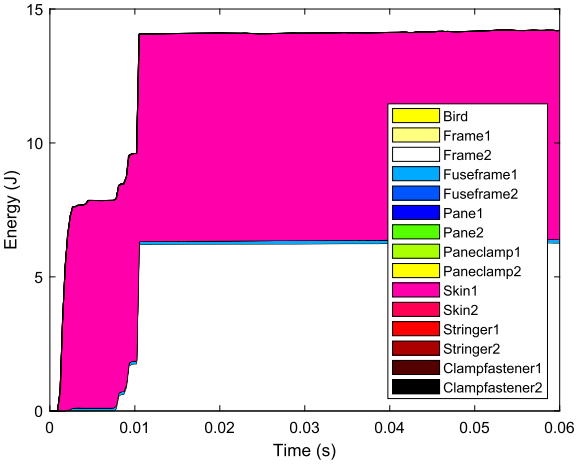

Fig. 44. Fuselage frame centre impact ALLPD contributors.

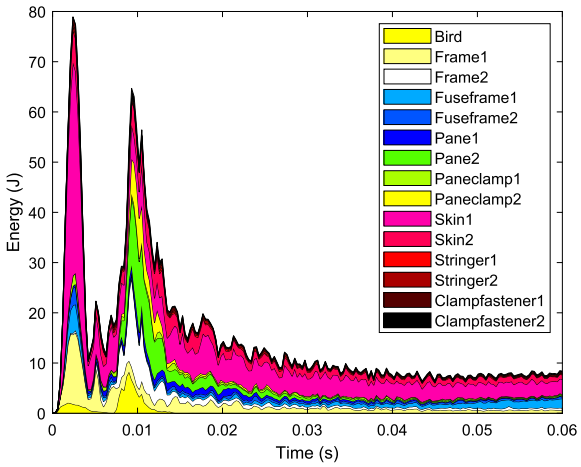

Fig. 45. Centre impact ALLSE contributors.

Table 17
Weight calculation of the total model using the baseline component thickness.

Component	Area (m^2)	Density (kg/m^3)	Baseline Thickness (mm)	Baseline Weight (kg)
2×Skin	0.52	2770	2.5	7.202
2×Window Frame	0.241	2800	3	4.0488
2×Pane Clamp	0.141	2800	3	2.3688
2×Pane	0.133	1200	9.6	3.06432
2×Clamp Fastener	0.095	2800	2	1.064
2×Fuselage Frame	0.117	2770	2.5	1.62045
2×Fuselage Frame Shear Clip	0.064	2770	2.5	0.8864
2×Stringer	0.082	2770	2.5	1.1357

To conclude, the critical impact location within the three study groups are location 1 for the horizontal impact, location 6 for the vertical impact, and location 15 for the diagonal impact. Among those three points and the fuselage frame impact points, location 6 has the highest amount of plastic energy with a value of approximately 370 J. Location 6 is therefore determined as the critical impact point of the Flying-V leading-edge fuselage. The energy contribution for each ALLPD and ALLIE structural element at location 6 is shown in Fig. 54 and Fig. 55. The window frame (yellow), polycarbonate pane, pane clamp, and fuselage skin are the main contributors to the plastic strain energy, while the pane clamp has the highest value. The impact history of location 6 is shown in Fig. 56.

3.4.3. Reduced integration - hourglass mode

In all the sub-component simulations, the reduced integration is turned off. It is essential to mention that the default setting in Abaqus has reduced integration turned on. When the reduced integration is turned on, hourglass modes may occur to the linear finite elements during element in-plane bending or twist warping. Although there is excessive element deformation that requires energy, the internal energy of the element has not changed. The artificial strain energy (ALLAE) is added in ALLIE as the energy for element deformation that is not recorded due to the hourglass effect. The hourglass effect is eliminated by turning off reduced integration, making the stress and strain results more accurate. The ratio of artificial strain energy to internal energy (ALLAE/ALLIE) should be below 5% to obtain a reliable output result [25]. A more rigorous criterion that the authors recommend is to keep this ratio below 2%. The ratio of ALLAE to ALLIE is shown in Fig. 57, which remains below 2% throughout the impact history when reduced integration is turned off. The small residual value of about 0.5% comes from the drilling penalty factor used in the shell formulation. The authors recommend turning off the reduced integration option when performing bird strike simulations, although resulting in computationally more expensive simulations. Whenever reduced integration is to be used, one should first evaluate whether the accuracy of the results generated by reduced integration is accepted by observing the criterion (ALLAE/ALLIE) lower than 2%.

3.4.4. Sensitivity analysis

The critical impact location identified for the Flying-V, location 6, is chosen for the sensitivity analysis. An additional fuselage frame and the shear clip are added at the section 1 edge shown in Fig. 58 since there should be a fuselage frame structure at that location during operation. Adding those stiff structure components could decrease the plastic strain energy ALLPD by 15%, as shown in Fig. 59.

The sensitivity analysis is done by adjusting the thickness for one structural component at a time to examine the values of the total model weight and ALLPD history in the model. The weight of the total model is calculated using Table 17 as an example for the baseline geometry, noting that the times two appear at the first column because there are two components in the model. The baseline thicknesses are the thickness values defined in Table 9. The baseline weight is the multiplication of the area density and thickness.

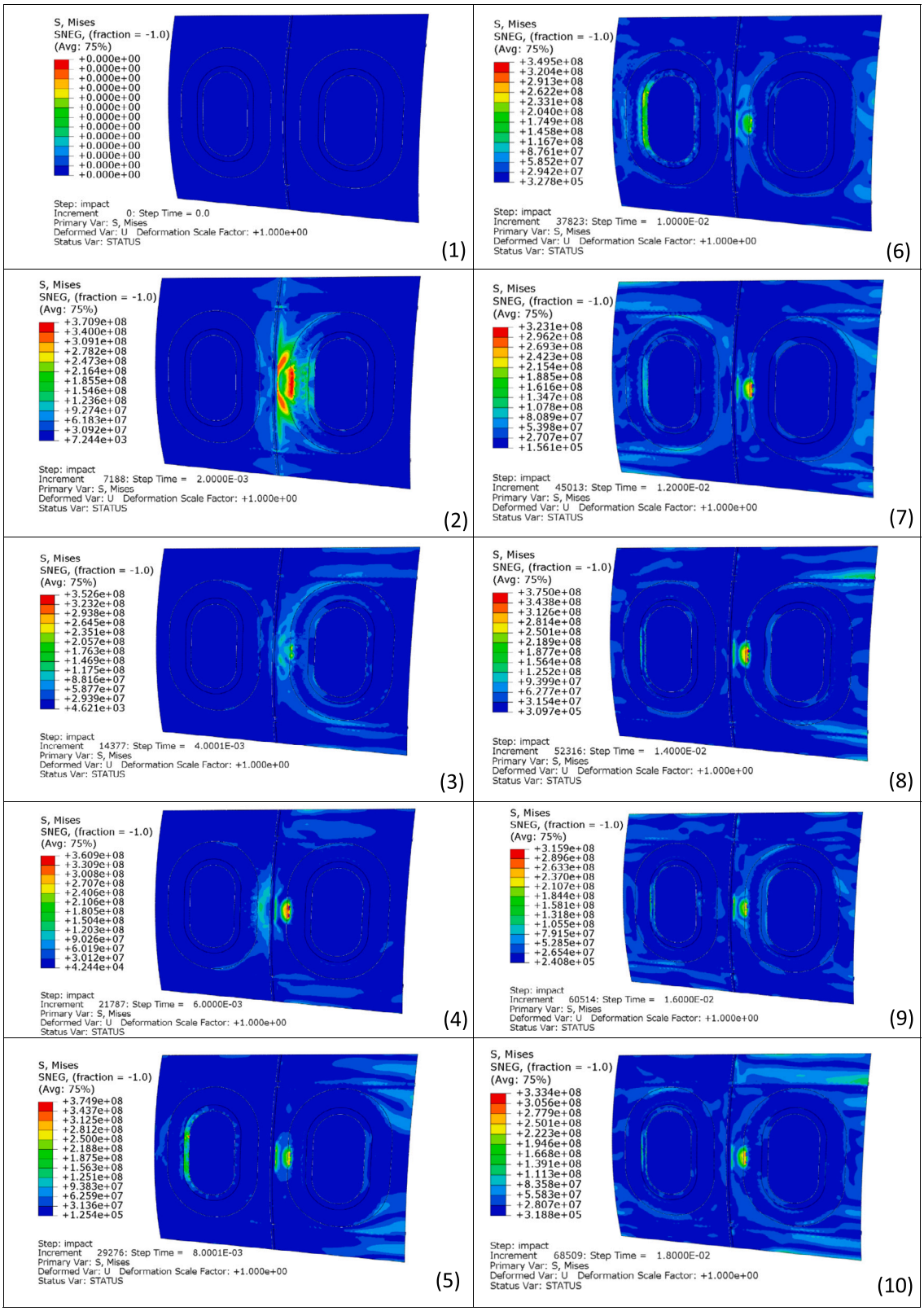

Fig. 46. Impact sequence of the fuselage frame's centre impact. The frames (1) to (10) are the impact sequence with a 2 ms time interval.

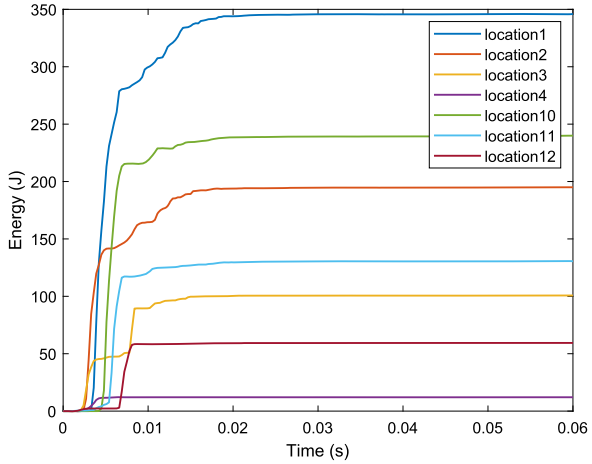

Fig. 47. ALLPD horizontal impact location comparison.

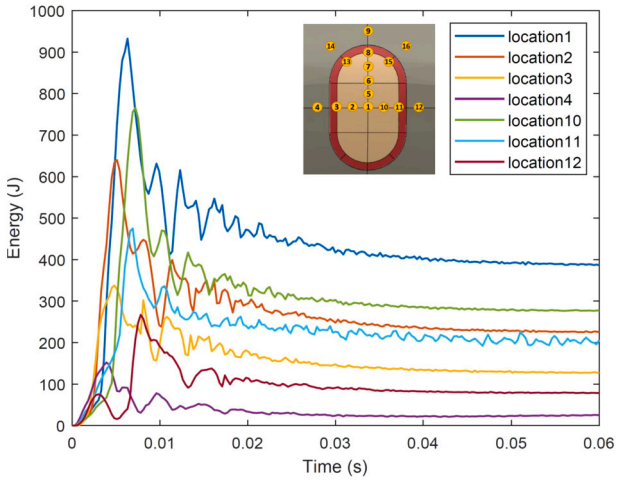

Fig. 48. ALLIE horizontal impact location comparison.

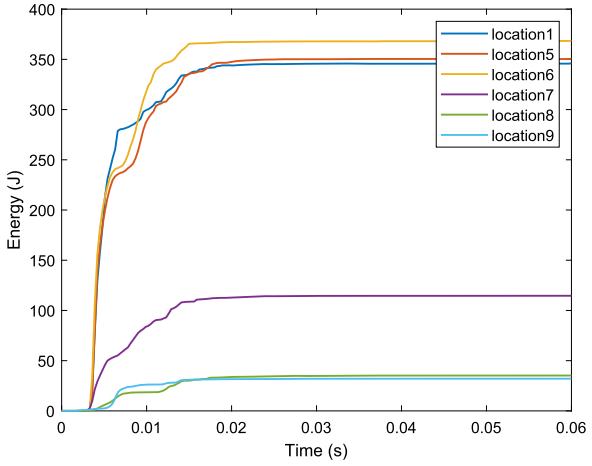

Fig. 49. ALLPD vertical impact location comparison.

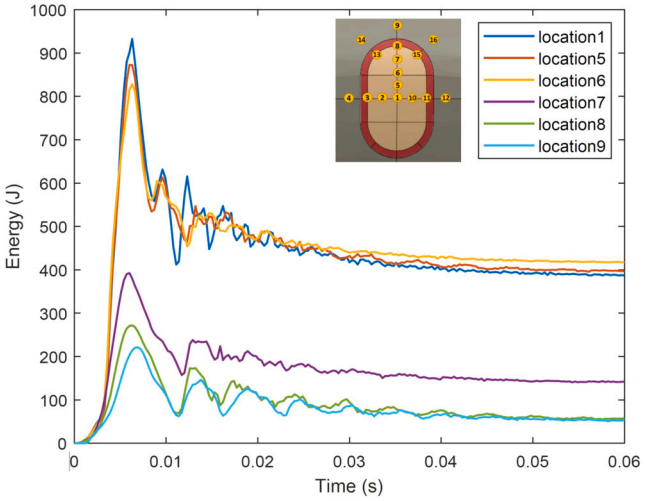

Fig. 50. ALLIE vertical impact location comparison.

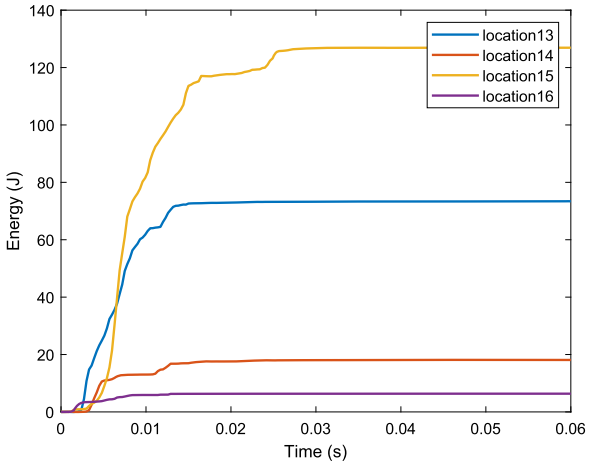

Fig. 51. ALLPD diagonal impact location comparison.

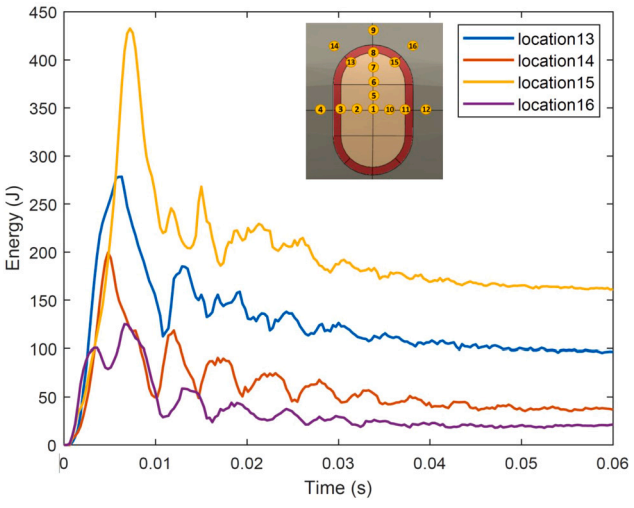

Fig. 52. ALLIE diagonal impact location comparison.

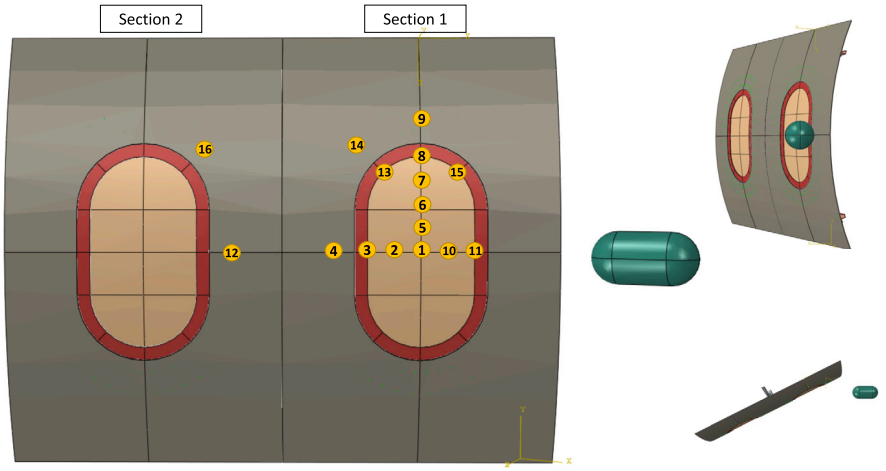

Fig. 53. Passenger window 16 impact locations (updated) study.

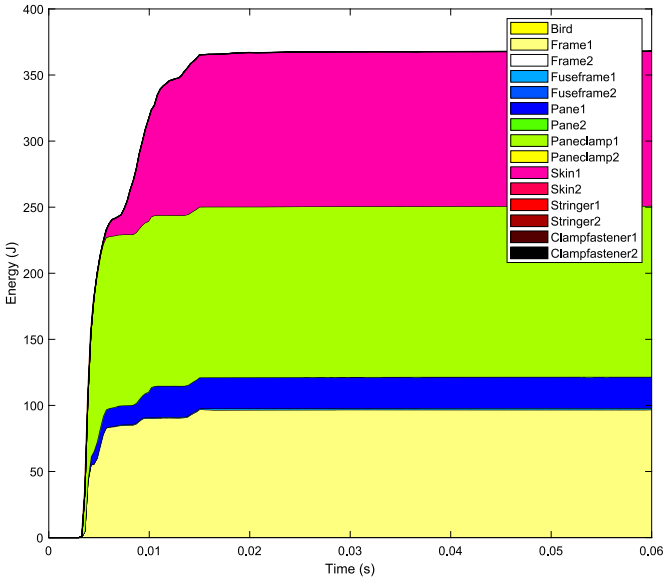

Fig. 54. Location 6, critical impact point ALLPD contributors.

Table 18
Thickness variables for the sensitivity study.

(mm)	Baseline Thickness	Thickness 2	Thickness 3	Thickness 4	Thickness 5
Skin	2.5	3.125	3.75	4.375	5
Window Frame	3	3.75	4.5	5.25	6
Pane Clamp	3	3.75	4.5	5.25	6

Table 19
Total model weight calculated by the component's adjusted thickness.

Total model weight (kg)	Baseline Thickness	Thickness 2	Thickness 3	Thickness 4	Thickness 5
Skin variable	21.39	23.19	24.99	26.79	28.59
Window frame variable	21.39	22.40	23.41	24.43	25.44
Pane Clamp variable	21.39	21.98	22.57	23.17	23.76

In the weight sensitivity analysis, 5 (five) thickness variables are applied, including the first baseline thickness. Three structural components are used to study the sensitivity, the skin, the window frame, and the pane clamp. Their 5 (five) thicknesses are shown in Table 18. The total model weight calculated is shown in Table 19. Using Table 19, the weight sensitivity for each component is plotted in Fig. 60.

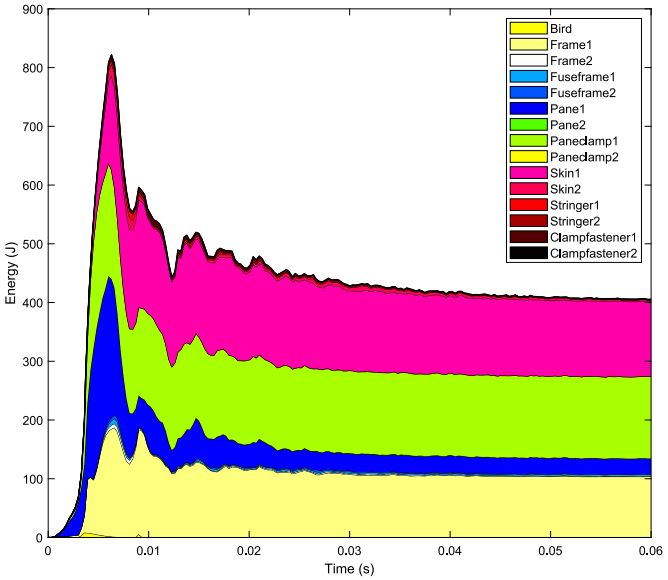

Fig. 55. Location 6, critical impact point ALLIE contributors.

The weight sensitivity is correlated with the surface area of the components. Since the fuselage has the highest surface area, it has the highest weight sensitivity. For each varied component thickness, a simulation is performed in which the maximum ALLPD value is retrieved from the ALLPD history plots. The plastic energy sensitivity to the component thickness is shown in Fig. 61.

From Fig. 61, it is shown that the ALLPD of the skin component is least sensitive to the thickness increase, which has the highest effect on the weight. Therefore, increasing the skin weight to reduce plasticity will increase weight and be ineffective in lowering plastic behaviour under bird strike. The highest plastic energy sensitivity is about the thickness of the pane clamp, indicating that reinforcing the structure that clamps the pane can decrease plasticity effectively. Interestingly, the pane clamp thickness has the lowest effect on the weight, yet another reason to be the recommended component for thickness increment. The authors investigated a case where the pane clamp thickness is increased by a factor of two, not yet leading to a plasticity-free design, but instead decreasing the plasticity by 50%.

A method to decrease plasticity is applying different thickness combinations by increasing the window frame and the pane clamp's thickness. To apply this method, the window frame thickness is chosen as 3.75 mm and the pane clamp as 5.25 mm since higher thickness did not significantly decrease plasticity. Combining the two components with the designated thickness showed in Fig. 62 that the ALLPD can be further reduced to 80 J, a 74.6% reduction compared to the original component thickness. Although the model is not plastic-free, a significant plasticity decrease is achieved. Further improvement in the plasticity behaviour is not pursued in the present study, which could be achieved by extending the methodology herein developed and applying it within an optimisation framework. Nevertheless, sensitivity analyses such as the one herein performed are of utmost importance to gain insight into the design and possible directions of improvement.

3.5. High-speed impact speed

A 4 lb bird with an impact speed of 133.38 m/s, the cruising speed of the Flying-V at 37000 ft, is simulated using the improved model obtained from the sensitivity analysis. Fig. 63 shows that the window has a large displacement and even that penetration occurred. Since this is an extreme impact scenario, only the damage mode is presented, and no further attempts to improve the design are performed. Possible solutions that could have been further investigated for this observed penetration are: fasten the polycarbonate pane with fasteners; apply adhesive before clamping the window pane.

4. Conclusions

A simulation model design was proposed for the Flying-V wing-fuselage windows, which are exposed to the flight direction and subject to a bird strike. The bird model herein adopted consisted of a smoothed particle hydrodynamics (SPH) model using gelatin material properties to simulate the bird's constitutive behaviour. During a bird strike on the passenger window, the impact location above and below the window pane's centre was the most critical, showing maximum plastic deformation. During a bird strike on the fuselage where the fuselage frame is located, the centre of the leading edge is the most crucial impact location.

The fuselage skin, window frame, and pane clamp are used for the weight and plastic energy sensitivity analysis. The pane clamp thickness showed the highest plasticity sensitivity and doubling its thickness resulted in a 50% decrease in the maximum plastic energy to 150 J. Further reduction in the plastic deformation was achieved by increasing the thicknesses of the pane clamp and the

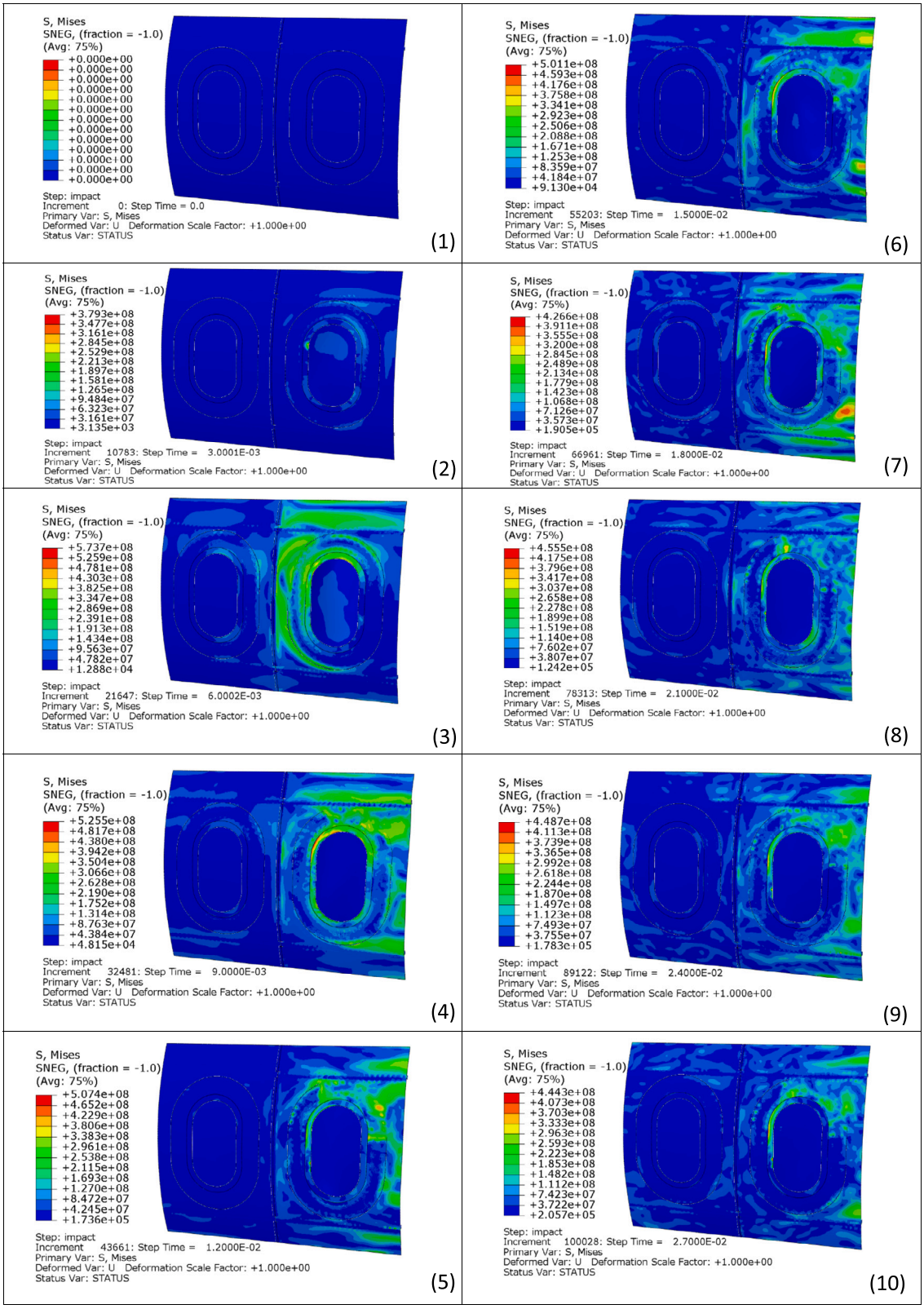

Fig. 56. Critical impact location 6's impact sequence (1) to (10) with a time interval of 3 ms.

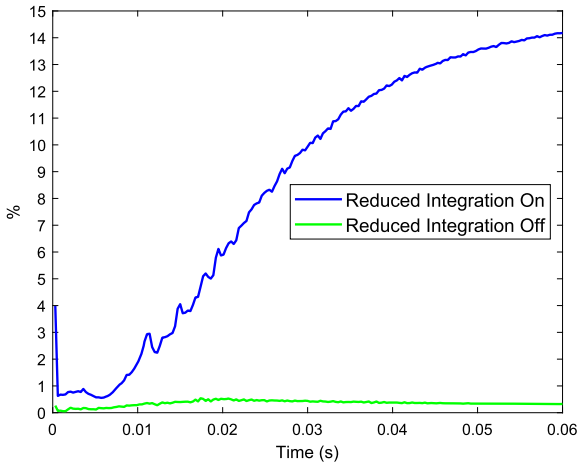

Fig. 57. Artificial strain energy to elastic strain energy ratio.

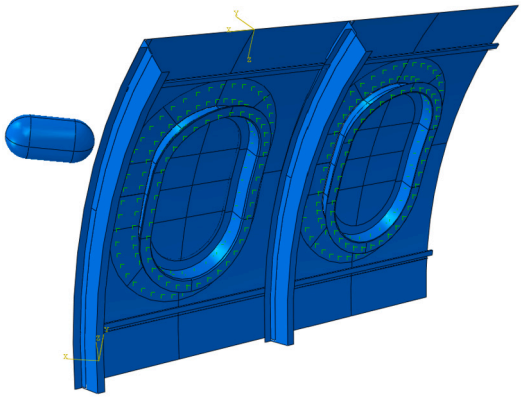

Fig. 58. Model for sensitivity analysis with two fuselage frames.

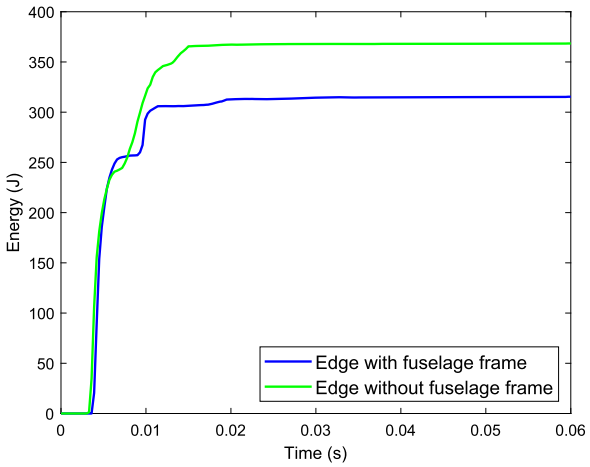

Fig. 59. ALLPD comparison for adding fuselage at section 1 edge. Adding a frame at the edge can decrease maximum plastic energy by 15%.

window frame. By increasing the window frame thickness from 3 mm to 3.75 mm, and the pane clamp from 3 mm to 5.25 mm, the plasticity energy decreases 74.6%. Although the obtained design was not plasticity-free, using the sensitivity analysis results reduced the design's plastic energy by a total of 80%. The improved design was impacted with a 4 lb bird with a velocity 0f 133 m/s, the cruising speed of the Flying-V at 37000 ft. This altitude is the highest bird strike altitude ever recorded, showing a critical

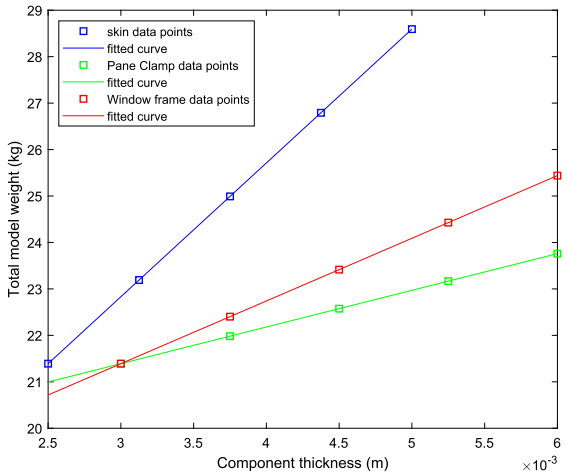

Fig. 60. Total model weight sensitivity to Component thickness.

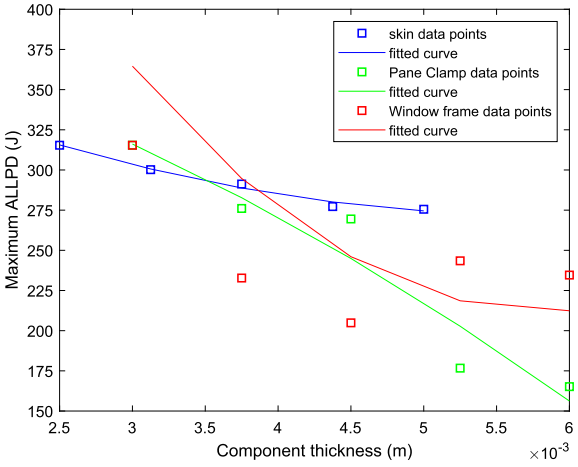

Fig. 61. ALLPD sensitivity to Component thickness.

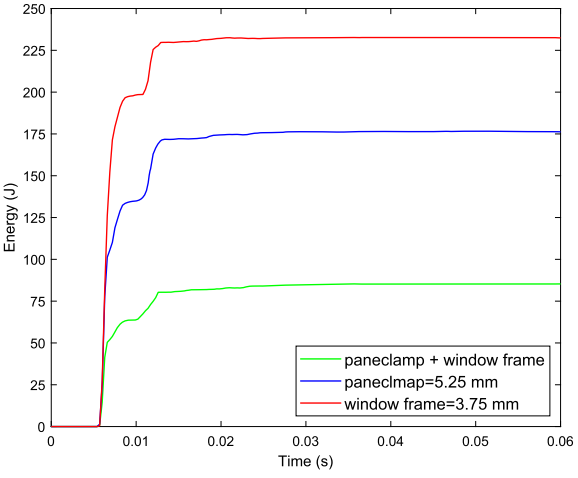

Fig. 62. Combining the thickness of the pane clamp and the window frame can further decrease ALLPD compared to the thickness increment of single components.

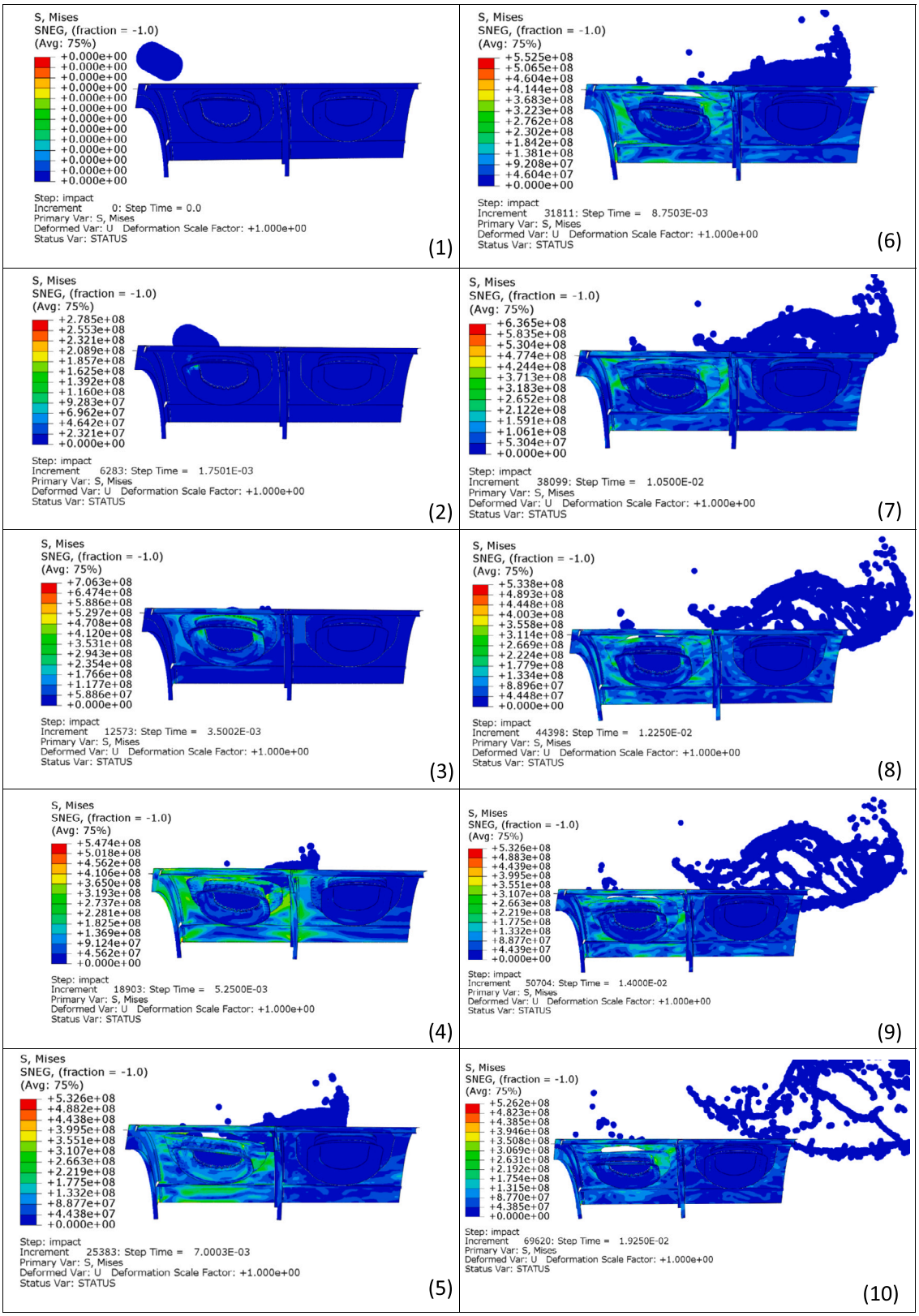

Fig. 63. Passenger window penetration with a 133 m/s impact. (1) to (10) with a time interval of 1.75 ms.

impact scenario for which the passenger window was penetrated. Therefore, further analysis and design iterations are required before reaching a feasible design for the Flying-V.

Recommendations for future work

The building block approach presented herein will be further developed and coupled within an optimisation framework to automate the design changes performed by sensitivity analyses. Every change in the geometry requires a re-designation of the material, section assignments, surface, geometry, and node sets. Every change in the thickness of the component requires the translation of the components to avoid overlapping the rendered shell thickness. An automatic method should be developed to decrease the modelling time during automated design iterations.

Physical testing at the element level and the detailed level should be performed to validate the proposed simulation models. Since testing requires more time and budget investment than simulation, funded research will be required for such activities.

It is recommended to break down the window frame, pane clamp, and clamp fastener components into a number of flanges and perform a more extensive sensitivity analysis and optimisation capability. Such design parameterisation should allow changing the length and thickness of the flanges, for instance. In addition, fastening the window pane to the window frame rather than having it clamped is a design modification expected to improve the 133 m/s high-speed impact.

Funding statement

This research did not receive any specific grant from funding agencies in the public, commercial, or not-for-profit sectors.

CRediT authorship contribution statement

Sian Ying Chen: Performed the experiments; Analyzed and interpreted the data; Wrote the paper.
Wydo van de Waerdt, Saullo G. P. Castro: Conceived and designed the experiments.

Declaration of competing interest

The authors declare no competing interests.

Data availability

Data included in article/supp. material/referenced in article.

Acknowledgements

Fokker Aerostructures B.V. and the Faculty of Aerospace Engineering at Delft University of Technology support this research study. The authors would like to thank all those who contributed their aid to this project. Roelof Vos for leading the development of the Flying-V configuration at TU Delft. Boyang Chen, Luc Kootte, and Jan Hol for solving issues of Abaqus running on the TU Delft cluster service.

References

[1] Agency E.U.A.S., Certification specifications and acceptable means of compliance for large aeroplanes cs-25, https://www.easa.europa.eu/downloads/121128/en8, 2020.
[2] Agency E.U.A.S., Proposed certification memorandum on modelling & simulation – CS-25 structural certification specifications, https://www.easa.europa.eu/en/downloads/116479/en, 2020.
[3] T. Belytschko, W.K. Liu, B. Moran, K. Elkhodary, Nonlinear Finite Elements for Continua and Structures, 2nd ed., John Wiley & Sons Ltd., 2014, https://www.wiley.com/en-us/Nonlinear+Finite+Elements+for+Continua+and+Structures%2C+2nd+Edition-p-9781118632703#description-section.
[4] J. Benad, Design of a commercial aircraft for high-subsonic speed as a flying wing configuration, Msc thesis. Technical, University of Berlin, Berlin, 2015.
[5] K. Cao, Y. Wang, Y. Wang, Experimental investigation and modeling of the tension behavior of polycarbonate with temperature effects from low to high strain rates, Int. J. Solids Struct. 51 (2014) 2539–2548, https://doi.org/10.1016/j.ijsolstr.2014.03.026.
[6] S.Y. Chen, W. van de Waerdt, S.G.P. Castro, Data set for design for bird strike crashworthiness using a building block approach applied to the Flying-V aircraft, https://doi.org/10.5281/zenodo.7270376, 2022.
[7] T. Dotman, A Structural Sizing Methodology for the Wing-Fuselage of the Flying-V, Ph.D. thesis, Delft University of Technology, 2021, http://resolver.tudelft.nl/uuid:69e21e65-7168-4f83-abf5-b646bb4c7fe5.
[8] R. Doubrava, M. Oberthor, P. Belsky, J. Raska, Bird and hail stone impact resistance analysis on a jet engine composite air inlet, MATEC Web Conf. 188 (2018) 04006, https://doi.org/10.1051/matecconf/201818804006.
[9] R. Doubrava, M. Oberthor, P. Bělský, B. Cabrnoch, Application of bird-strike verified analysis for the design of fast helicopter composite Cowling, Int. J. Struct. Integrity 13 (2022) 649–658, https://doi.org/10.1108/IJSI-10-2021-0113.
[10] A.F. El-Sayed, Bird Strike in Aviation: Statistics, Analysis and Management, John Wiley & Sons Ltd., 2019, https://search.ebscohost.com/login.aspx?direct=true&scope=site&db=nlebk&db=nlabk&AN=2141844.
[11] S. Fu, Y. Wang, Y. Wang, Tension testing of polycarbonate at high strain rates, Polym. Test. 28 (2009) 724–729, https://doi.org/10.1016/j.polymertesting.2009.06.002.

[12] V. Goyal, C. Huertas, J. Borrero, T. Leutwiler, Robust Bird-Strike modeling based on ALE formulation using LS-DYNA, in: 47th AIAA/ASME/ASCE/AHS/ASC Structures, Structural Dynamics, and Materials Conference 14th AIAA/ASME/AHS Adaptive Structures Conference 7th, American Institute of Aeronautics and Astronautics, Reston, Virigina, 2006, http://arc.aiaa.org/doi/abs/10.2514/6.2006-1759.
[13] V. Goyal, C. Huertas, T. Leutwiler, J. Borrero, T. Vasko, Robust Bird-Strike modeling based on SPH formulation using LS-DYNA, in: 47th AIAA/ASME/ASCE/AHS/ASC Structures, Structural Dynamics, and Materials Conference 14th AIAA/ASME/AHS Adaptive Structures Conference 7th, American Institute of Aeronautics and Astronautics, Reston, Virigina, 2006, https://doi.org/10.2514/6.2006-1878.
[14] S. Heimbs, T. Wagner, H. Meister, C. Brand, M. Calomfirescu, Bird strike on aircraft radome: dynamic characterisation of quartz fibre composite sandwich for accurate, predictive impact simulations, EPJ Web Conf. 183 (2018) 01007, https://doi.org/10.1051/epjconf/201818301007.
[15] Institute, B.M., Administration, U.F.A., Administration, U.S.F.A., Administration, É.U.F.A., Laboratories, B.M.I.C., (U.S.), W.J.H.T.C., of Defense, U.D., of Defense, U.S.D., of Defense, É.U.D., Aeronautics, U.N., Administration, S., et al., 2016. Metallic Materials Properties Development and Standardization (MMPDS): MMPDS-11, July 2016. Federal Aviation Administration. https://books.Google.nl/books?id=Ng9EAQAACAAJ.
[16] M. Kendall, C. Siviour, Experimentally simulating high-rate behaviour: rate and temperature effects in polycarbonate and pmma, Philos. Trans. R. Soc. A, Math. Phys. Eng. Sci. 372 (2014) 20130202, https://doi.org/10.1098/rsta.2013.0202.
[17] Mitsubishi Aircraft Corporation-Aichi (JP), T.Y., Aircraft window, https://patents.google.com/patent/US9415854?oq=12178442.5, 2012.
[18] C. Niu, M. Niu, Airframe Structural Design: Practical Design Information and Data on Aircraft Structures. Airframe Book Series, Adaso Adastra Engineering Center, 1999, https://books.google.nl/books?id=yT15SwAACAAJ.
[19] L.S. Nizampatnam, Models and methods for bird strike load predictions, PhD thesis, https://soar.wichita.edu/handle/10057/1494, 2007.
[20] W. Oosterom, Flying-V family design https://repository.tudelft.nl/islandora/object/uuid%3A9e8f9a41-8830-405d-8676-c46bf6b07891, 2021.
[21] A. Plast, Transparent products – polycarbonate sheets makroclear™, https://arlaplast.com/wp-content/uploads/2021/05/Datasheet-Makroclear-2014-EN-v1.pdf, 2014.
[22] M.S. Reza Hedayati (Ed.), Bird Strike an Experimental, Theoretical, and Numerical Investigation. 2 - Statistics, Woodhead Publishing, 2016, https://doi.org/10.1016/B978-0-08-100093-9.00002-9.
[23] M.S. Reza Hedayati (Ed.), Bird Strike an Experimental, Theoretical, and Numerical Investigation. 6 - Finite Element Bird Strike Modeling, Woodhead Publishing, 2016, https://doi.org/10.1016/B978-0-08-100093-9.00002-9.
[24] S. Ritt, Sae g-28 simulants for impact and ingestion – technical strategy, 2021.
[25] M. Smith, ABAQUS/standard user's manual, version 6.9, in: Dassault Systèmes Simulia Corp, United States, 2009.
[26] A. Tudor, Bird ingestion research at rolls-royce(aircraft gas turbine engine damage from bird ingestion, discussing bird simulation tests, flight hazards and engine design implications), 1968.
[27] A.S. Verma, S.G. Castro, Z. Jiang, J.J. Teuwen, Numerical investigation of rain droplet impact on offshore wind turbine blades under different rainfall conditions: a parametric study, Compos. Struct. 241 (2020) 112096, https://doi.org/10.1016/j.compstruct.2020.112096.
[28] J.S. Wilbeck, Impact behavior of low strength projectiles, Ph.D. thesis, Texas A&M University, 1977.
[29] Y. Xu, T. Gao, J. Wang, W. Zhang, Experimentation and modeling of the tension behavior of polycarbonate at high strain rates, Polymers 8 (2016), https://doi.org/10.3390/polym8030063.